Galaxy Stellar Mass Functions from $z \sim 10$ to $z \sim 6$ using the Deepest Spitzer/Infrared Array Camera Data: No Significant Evolution in the Stellar-to-halo Mass Ratio of Galaxies in the First Gigayear of Cosmic Time

Mauro Stefanon[1] , Rychard J. Bouwens[1] , Ivo Labbé[2] , Garth D. Illingworth[3] , Valentino Gonzalez[4,5] , and
Pascal A. Oesch[6,7]
[1] Leiden Observatory, Leiden University, NL-2300 RA Leiden, The Netherlands; stefanon@strw.leidenuniv.nl
[2] Centre for Astrophysics and SuperComputing, Swinburne, University of Technology, Hawthorn, Victoria, 3122, Australia
[3] UCO/Lick Observatory, University of California, Santa Cruz, 1156 High St, Santa Cruz, CA 95064, USA
[4] Departamento de Astronomía, Universidad de Chile, Casilla 36-D, Santiago 7591245, Chile
[5] Centro de Astrofísica y Tecnologias Afines (CATA), Camino del Observatorio 1515, Las Condes, Santiago 7591245, Chile
[6] Departement d'Astronomie, Université de Genéve, 51 Ch. des Maillettes, CH-1290 Versoix, Switzerland
[7] Cosmic Dawn Center (DAWN), Niels Bohr Institute, University of Copenhagen, Jagtvej 128, København N, DK-2200, Denmark

Abstract

We present new stellar mass functions at $z \sim 6$, $z \sim 7$, $z \sim 8$, $z \sim 9$ and, for the first time, $z \sim 10$, constructed from ~ 800 Lyman-break galaxies previously identified over the eXtreme Deep Field and Hubble Ultra-Deep Field parallel fields and the five Cosmic Assembly Near-infrared Deep Extragalactic Legacy Survey fields. Our study is distinctive due to (1) the much deeper (~ 200 hr) wide-area Spitzer/Infrared Array Camera (IRAC) imaging at 3.6 μm and 4.5 μm from the Great Observatories Origins Deep Survey Re-ionization Era Wide-area Treasury from Spitzer program (GREATS) and (2) consideration of $z \sim 6$–10 sources over a $3\times$ larger area than those of previous Hubble Space Telescope+Spitzer studies. The Spitzer/IRAC data enable $\geqslant 2\sigma$ rest-frame optical detections for an unprecedented 50% of galaxies down to a stellar mass limit of $\sim 10^8 \mathcal{M}_\odot$ across all redshifts. Schechter fits to our volume densities suggest a combined evolution in the characteristic mass $\mathcal{M}^*$ and normalization factor ϕ^* between $z \sim 6$ and $z \sim 8$. The stellar mass density (SMD) increases by $\sim 1000\times$ in the ~ 500 Myr between $z \sim 10$ and $z \sim 6$, with indications of a steeper evolution between $z \sim 10$ and $z \sim 8$, similar to the previously reported trend of the star formation rate density. Strikingly, abundance matching to the Bolshoi–Planck simulation indicates halo mass densities evolving at approximately the same rate as the SMD between $z \sim 10$ and $z \sim 4$. Our results show that the stellar-to-halo mass ratios, a proxy for the star formation efficiency, do not change significantly over the huge stellar mass buildup occurred from $z \sim 10$ to $z \sim 6$, indicating that the assembly of stellar mass closely mirrors the buildup in halo mass in the first ~ 1 Gyr of cosmic history. The James Webb Space Telescope is poised to extend these results into the "first galaxy" epoch at $z \gtrsim 10$.

1. Introduction

In the last decade, the increased sensitivity at near-infrared wavelengths provided by the Hubble Space Telescope (HST) Wide Field Camera 3 (WFC3) has revealed $\gtrsim 10k$ galaxies at $z \gtrsim 4$ (e.g., Bouwens et al. 2015; Finkelstein et al. 2015a), probing galaxy formation to epochs as early as $z \sim 10-12$, just ~ 400–500 Myr after the Big Bang (see, e.g., Bouwens et al. 2011a, 2013; Coe et al. 2013; Ellis et al. 2013; McLure et al. 2013; Oesch et al. 2014, 2016, 2018; Calvi et al. 2016; McLeod et al. 2016; Morishita et al. 2018; Salmon et al. 2018; Lam et al. 2019).

Despite the remarkable advances in the field, some uncertainties still exist on the estimates of fundamental parameters, such as the cosmic star formation rate density (CSFRD). A number of studies suggest that the CSFRD underwent a rapid increase in the first ~ 600 Myr, followed by a less rapid growth (see, e.g., Oesch et al. 2012, 2014, 2018; Ellis et al. 2013; Bouwens et al. 2015), consistent with the rate of growth of the dark matter halos (e.g., Oesch et al. 2018). Other works, however, indicate higher densities at $z \sim 8$–10 resulting in a reduced evolution of the CSFRD from $z \sim 9$ to $z \sim 4$ (e.g., McLure et al. 2013; McLeod et al. 2016; Bhatawdekar et al. 2019; Kikuchihara et al. 2020). Furthermore, the discovery of

enigmatic objects, such as GN-z11 (Oesch et al. 2016) and MACS1149-JD1 (Zheng et al. 2012; Hashimoto et al. 2018; Hoag et al. 2018), prompt questions about how such massive galaxies could assemble so rapidly.

A complementary approach to studying the assembly of galaxies consists of measuring the integral with cosmic time of the star formation rate (SFR), i.e., the stellar mass ($\mathcal{M}_\star$). Numerous studies have estimated the stellar mass function (SMF) and the stellar mass density (SMD) of galaxies to $z \sim 8$ (see Madau & Dickinson 2014 and references therein, and those we list in Section 7.2). These two approaches should yield consistent results. The emerging picture is that, from $z \sim 7$ to today, the evolution of the SMD is actually consistent with that expected from the integration of the CSFRD (modulo a systematic offset of ~ 0.2–0.5 dex—see, e.g., Madau & Dickinson 2014; Leja et al. 2019 and references therein).

At higher redshifts, the current estimates suggest a marginal evolution of the SMD for $8 \lesssim z \lesssim 9$ (e.g., Bhatawdekar et al. 2019; Kikuchihara et al. 2020) followed by a $\gtrsim 1$–1.5 dex drop by $z \sim 10$ (Oesch et al. 2014). Nevertheless, current SMF measurements at such high redshifts suffer from higher systematic uncertainties, both at the sample selection stage
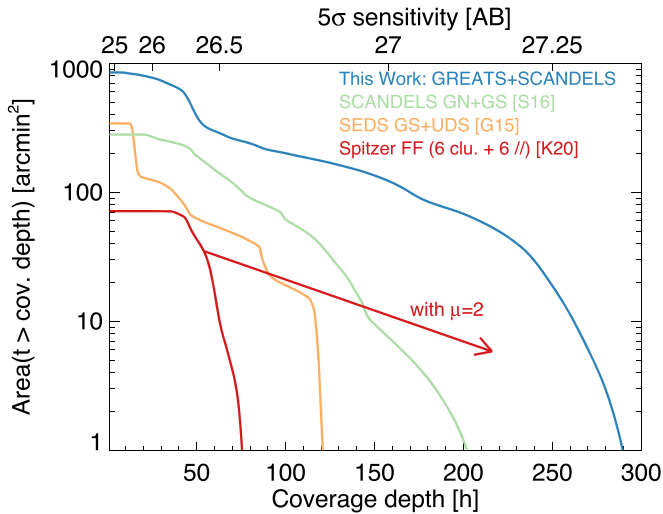
Figure 1. Cumulative area as a function of coverage depth (in hr) in the IRAC 3.6 μm band, for representative sets of observations recently adopted for the measurement of the SMF at $z \sim 6$ and above. Specifically, we include data from GREATS (Stefanon et al. 2021b), S-CANDELS (Ashby et al. 2015), SEDS (Ashby et al. 2013), and the Spitzer-Frontier Fields (Shipley et al. 2018). The top axis presents approximate point-source 5σ sensitivity from the SENS-PET calculator. The red arrow marks the effective depth that can be obtained when sources in the cluster fields are magnified by $\mu = 2$. The smaller area results from the decrease of effective area due to magnification (a factor ~ 6 for $z \sim 8$ sources when $\mu \geqslant 2$). In square brackets we indicate the studies with their adopted set of IRAC data: G15: Grazian et al. (2015; see also Duncan et al. 2014); S16: Song et al. (2016); K20: Kikuchihara et al. (2020; see also Bhatawdekar et al. 2019). The very substantial gains from the new GREATS + S-CANDELS data sets are apparent.

and in the estimates of stellar masses for individual sources, as we discuss below.

A number of recent papers have estimated SMFs from samples selected over areas ranging from $\sim$few $\times$ arcmin^2 to $\sim$100 arcmin^2 (e.g., Duncan et al. 2014; Grazian et al. 2015; Song et al. 2016; Bhatawdekar et al. 2019; Kikuchihara et al. 2020). Such small areas, however, introduce large cosmic variance, particularly at the massive end, with uncertainties from cosmic variance approaching $\sim$50% at $z \sim 7$–8 (see, e.g., Bhowmick et al. 2020; McLeod et al. 2021), while the corresponding small sample sizes for massive galaxies result in larger Poissonian uncertainties. The obvious solution, observations over $\sim$square-degree fields, provide stringent constraints on the high-mass end but lack sufficient depth to constrain the low-mass end (e.g., Davidzon et al. 2017). The lack of deep wide-field areas has been a challenge for deriving robust SMFs.

Robust estimates of stellar masses require detections in the rest-frame optical. At redshifts $z \gtrsim 5$ these can currently only be obtained by observations with Spitzer/Infrared Array Camera (IRAC) (Fazio et al. 2004). The current depths of IRAC data in extragalactic fields allow for individual detections of only the brightest, and hence most massive sources (see Figure 1). Consequently, spectral energy distributions (SEDs) in the optical at lower masses are still lacking, or at best quite uncertain, essentially restricting the derivation of the SMF to relatively massive systems at high redshifts (e.g., Duncan et al. 2014; Grazian et al. 2015; Song et al. 2016). Furthermore, the use of stacking to characterize the properties of fainter sources has only resulted in modest gains due to the small sample sizes (e.g., González et al. 2012; Song et al. 2016; Kikuchihara et al. 2020). An interesting exception to this limitation are recent studies based on the Hubble Frontier Field (HFF; Lotz et al. 2017)

initiative, which leverage the gravitational magnifications of low-z galaxy clusters to reach fainter limits at high redshifts (e.g., Bhatawdekar et al. 2019; Kikuchihara et al. 2020). Unfortunately, systematic uncertainties in the magnification maps (e.g., Bouwens et al. 2017) and the higher surface densities of nearby large and bright objects in these fields (e.g., Castellano et al. 2016; Merlin et al. 2016; Shipley et al. 2018) make it very difficult to carry out reliable photometry.

New IRAC data combined with Hubble observations now provide an opportunity to overcome the aforementioned challenges. In this work, we measure the galaxy SMF at $z \sim 6$–10 using the most comprehensive selection of $z \sim 6$–10 galaxies from the HST legacy fields, including galaxies from all five Cosmic Assembly Near-infrared Deep Extragalactic Legacy Survey (CANDELS) fields (Grogin et al. 2011; Koekemoer et al. 2011). Most importantly, new full-depth IRAC mosaics from the Great Observatories Origins Deep Survey (GOODS) Re-ionization Era Wide-area Treasury from Spitzer (GREATS; PI: I. Labbé—Stefanon et al. 2021b) allow us to determine their rest-frame optical fluxes. As we show in Section 4, these data provide $\geqslant 2\sigma$ detections in the IRAC 3.6 μm and 4.5 μm bands for 50% of individual sources in the sample down to stellar masses $\mathcal{M}_\star \sim 10^8 \mathcal{M}_\odot$, at all the redshifts considered for this study. Additionally, our galaxy SMFs leverage a search area that is $3\times$ larger than in previous studies, lessening both the impact of cosmic variance and Poisson noise (by $1.7\times$). The combination of the new GREATS data set and the large Hubble sample enables derivation of an SMF where sample statistics and cosmic variance are minimized, as well as provides the needed rest-frame optical SEDs for more accurate mass estimates.

A brief summary of the organization of this paper follows. In Section 2, we briefly describe the sample adopted for the SMF measurements. Section 3 details the procedures we followed to estimate the stellar mass of galaxies depending on the redshift bin and on the significance of the IRAC detections. In Section 4, we present the stellar mass-to-UV luminosity relation we derive from our stellar mass measurements, while in Section 5 we characterize the completeness of our sample. Section 6 includes a presentation of our new SMF determinations and compares these new results with others in the literature. In Section 7, we characterize the buildup of the SMD with cosmic time and connect our results to a similar buildup in the dark matter halo mass density and limited evolution in the stellar-to-halo mass ratios (SHMRs). In Section 8, we include a summary.

Throughout this paper, we adopt magnitudes in the AB system (Oke & Gunn 1983) and a ΛCDM cosmology with $\Omega_m = 0.3$, $\Omega_\Lambda = 0.7$, $H_0 = 70 \ \mathrm{km \ s^{-1} \ Mpc^{-1}}$, unless otherwise stated. Our stellar mass measurements assumed a Salpeter (1955) initial mass function (IMF). We conventionally denote the logarithm in base 10 with log.

2. Samples

For this study, we set out to derive the SMF in redshift bins centered at $z \sim 6$, 7, 8, 9, and 10. In the next sections. we outline our sample selection criteria, while in Tables 1 and 2 we summarize the main properties of the adopted data sets and of the resulting samples.

Table 1
Observational Data Used for the SMF Estimates

Field		Area (arcmin^2)	H_{160}[a] 5σ (mag)	IRAC Data[b]	3.6μ m[c] 5σ (mag)	4.5 μm[c] 5σ (mag)
Name						
XDF		4.7	29.4	GREATS	~27.2	~26.7
HUDF09-1		4.7	28.3	GREATS	~26.3	~25.8
HUDF09-2		4.7	28.7	GREATS	~27.0	25.5–26.0
ERS		40.5	27.4	GREATS	26.2–27.0	25.6–26.7
CANDELS	GOODS-N Deep	62.9	27.5	GREATS	27.0–27.3	26.5–26.8
	GOODS-N Wide	60.9	26.7	GREATS	26.3–27.2	25.8–26.8
	GOODS-S Deep	64.5	27.5	GREATS	~27.3	26.6–26.9
	GOODS-S Wide	34.2	26.8	GREATS	26.5–27.2	26.2–26.7
	COSMOS	151.9	26.8	SEDS+S-CANDELS	26.4–26.7	26.0–26.3
	EGS	150.7	26.9	SEDS+S-CANDELS	26.1–26.5	25.7–26.1
	UDS	151.2	26.8	SEDS+S-CANDELS	25.4–26.3	25.0–25.9
Total:		730.9				

Notes.
[a] 5σ limit from Bouwens et al. (2015), computed from the median of measured uncertainties of sources.
[b] GREATS: Stefanon et al. (2021b); SEDS: Ashby et al. (2013); S-CANDELS: Ashby et al. (2015).
[c] Nominal 5σ limit for point sources from the SENS-PET exposure time calculator, based on the exposure time maps. Due to inhomogeneities in the coverage, a range of values is quoted when the depth varies by more than ~0.2 mag across the field. Because of the combined effects of the broad Spitzer/IRAC PSF and the long exposure times, source blending may reduce the actual depth (see discussion in Labbé et al. 2015).

2.1. Samples at z ∼ 6, 7, and 8

Our goal was to make use of the largest and most comprehensive set of $z\sim$ 6, 7, and 8 galaxies from the CANDELS fields and assorted deep HST fields for the purposes of deriving galaxy SMFs. Specifically, the $z\sim$ 6, 7, and 8 samples we utilize are based on the I-, z-, and Y-dropouts, respectively, Bouwens et al. (2015) identified over the CANDELS (Grogin et al. 2011; Koekemoer et al. 2011), GOODS-N, GOODS-S (Giavalisco et al. 2004), Ultra Deep Survey (UDS) (Lawrence et al. 2007), and Cosmological Evolution Survey (COSMOS) (Scoville et al. 2007) fields, the Early Release Science (ERS) field (Windhorst et al. 2011), and the Ultra Deep Field (UDF)/eXtreme Deep Field (XDF) (Beckwith et al. 2006; Ellis et al. 2013; Illingworth et al. 2013) with the HUDF09-1 and HUFD09-2 parallels (Bouwens et al. 2011b). We also included the $z\sim$ 6 candidates Bouwens et al. (2015) identified over the CANDELS Extended Groth Strip (EGS) field (Davis et al. 2007), but not the $z\sim$ 7–8 candidates from this field given the lack of deep Y-band imaging to segregate galaxies at $z\sim$ 7 from those at $z\sim$ 8.

The CANDELS fields have received substantial coverage with Spitzer/IRAC (Fazio et al. 2004), in particular at 3.6 μm and 4.5 μm. Starting at $z\sim$ 5, these bands probe the rest-frame optical, pivotal for the estimates of stellar masses. Furthermore, the evolution with redshifts of the [3.6] − [4.5] color suggests contributions by strong emission lines, such as [O II]λ3727, [O III]$\lambda\lambda$4959, 5007, Hα, and Hβ. Inclusion of these lines into the fitting process can greatly improve the accuracy of the photometric redshifts (e.g., Smit et al. 2014; Roberts-Borsani et al. 2016) and better discriminate against lower redshift interlopers.

Most importantly, and a crucial addition to the goals of this study, the GOODS-N and GOODS-S fields benefit from new full-depth Spitzer/IRAC 3.6 μm and 4.5 μm imaging from the GREATS program (PI: I. Labbé—Stefanon et al. 2021b). GREATS increases the integration time to $\gtrsim$200 hr over an area of ~100 arcmin^2 while improving the homogeneity in both 3.6 μm and 4.5 μm depths. The corresponding IRAC point-

source 5σ sensitivity of ~27.2 mag approximately matches the HST H_{160} flux density limits from CANDELS.

For the EGS, UDS, and COSMOS fields, we included observations from the S-CANDELS program (Ashby et al. 2015), which, in combination with the Spitzer Extended Deep Survey (SEDS) program (Ashby et al. 2013), provides a coverage of $\gtrsim$50 hr per field (nominal SENS-PET[8] 5σ limits for point sources of ~26.0–26.4 mag at 3.6 μm and 4.5 μm, respectively).

Figure 1 presents the cumulative area as a function of the integration time for the mosaics adopted in our study and for few other prior IRAC data sets that have been used in recent SMF determinations at $z > 6$ (Duncan et al. 2014; Grazian et al. 2015; Song et al. 2016; Bhatawdekar et al. 2019 and Kikuchihara et al. 2020). Our data are $\gtrsim$2× deeper over the GOODS fields and reach ~3× more area thanks to the combination of all the CANDELS fields. The IRAC data adopted in our study provide moderate to high signal-to-noise ratio (S/N) information for a large fraction of sources in our sample (we further discuss this in Section 5).

We extracted new flux densities from the GREATS and S-CANDELS mosaics for all sources in our sample using the deblending code MOPHONGO (Labbé et al. 2006, 2010a, 2010b, 2013, 2015). In Figure 2, we present image stamps of three $z\sim$ 7–8 sources as they appear in the ~70 hr-deep IRAC mosaics from SEDS and in the ~200 hr regions of GREATS. In the same figure, we also show the residuals after subtracting their neighbors with MOPHONGO adopting first an average point-spread function (PSF) and then the PSF reconstructed accounting for the specific orientations of the IRAC observations over the corresponding regions (as pioneered in earlier work by Labbé et al. 2015). It is evident from the last two columns of Figure 2 how, not only the photometric depth, but also an accurate knowledge of the PSF, are of crucial importance for a robust flux density estimate using Spitzer data.

---

[8] http://ssc.spitzer.caltech.edu/warmmission/propkit/pet/senspet/

Table 2
Number of Sources in the Samples Used for Our SMF Measurements

Field		# Sources[a]				
Name		$z \sim 6$	$z \sim 7$	$z \sim 8$	$z \sim 9$	$z \sim 10$
XDF		30 (17)	7 (3)	8 (5)	6 (1)	2 (0)
HUDF09-1		15 (4)	7 (1)	3 (0)	0	0
HUDF09-2		11 (7)	6 (2)	2 (1)	1 (1)	0
ERS		38 (30)	15 (14)	2 (0)	1 (1)	0
CANDELS	GOODS-N Deep	89 (73)	70 (47)	14 (5)	2 (2)	2 (1)
	GOODS-N Wide	51 (41)	24 (19)	10 (6)	0	1 (1)
	GOODS-S Deep	114 (90)	37 (23)	15 (11)	1 (1)	1 (1)
	GOODS-S Wide	36 (31)	6 (5)	0	1 (1)	0
	COSMOS	37 (33)	15 (12)	5 (5)	1 (1)	0
	EGS	71 (62)	…[b]	…[b]	5 (5)	0
	UDS	31 (28)	17 (16)	6 (5)	1 (1)	0
Totals:		523 (416)	204 (142)	65 (38)	19 (14)	6 (3)

Notes.
[a] Number of sources selected in each redshift bin. The quantities in parentheses indicate the number of sources with S/N > 2 in the IRAC bands.
[b] We excluded the $z \sim 7$ and $z \sim 8$ samples in EGS because Bouwens et al. (2015) used the IRAC data themselves (given the lack of deep Y-band data for this field) to help with the selection of these sources and thus there are large uncertainties on the photometric redshifts of $z = 7$–8 sources from the EGS field.

We redetermined the photometric redshifts of our sample with EAZY (Brammer et al. 2008), complementing the standard template set with templates extracted from the Binary Population and Spectral Synthesis code (BPASS; Eldridge et al. 2017) v1.1 for metallicity $Z = 0.2Z_\odot$. We incorporated nebular lines with equivalent widths EW(H α) $\sim$ 1000–3000Å and line ratios from Anders & Fritze-v. Alvensleben (2003), as these extreme EWs reproduce the observed [3.6]–[4.5] colors for many spectroscopically confirmed $z \sim 7$–9 galaxies (Ono et al. 2012; Finkelstein et al. 2013; Oesch et al. 2015; Zitrin et al. 2015; Roberts-Borsani et al. 2016; Stark 2016). Driven by recent observational results (e.g., Oesch et al. 2015; Zitrin et al. 2015; Roberts-Borsani et al. 2016; De Barros et al. 2017; Stark et al. 2017), we removed the Lyα line from those templates that had EW(Lyα)>40 Å. We also included templates of 2 Gyr old, passively evolving systems from Bruzual & Charlot (2003), with Calzetti et al. (2000) extinction in the range $A_V = 0$–8 mag to test the robustness of our selected candidates against being lower-redshift interlopers that were highly attenuated by dust. To further improve the robustness of the $z \sim 6$, 7 and $z \sim 8$ samples, we required the integral of the redshift likelihood (equivalent to a posterior probability assuming a uniform prior) to be $p(z) > 0.6$ beyond $z = 5$, 6, and 7, and the peak of the $p(z)$ to lie within the ranges $5.5 \leqslant z_{phot} < 6.3$, $6.3 \leqslant z_{phot} < 7.5$ and $7.5 \leqslant z_{phot} < 8.5$ for the samples at $z \sim 6$, 7 and $z \sim 8$, respectively. These constraints had a modest impact on the final sizes of our samples removing $22 \pm 5\%$ and $25 \pm 10\%$ ($p(z)$ and z_{phot} selections, respectively). After applying these criteria, our samples included 789, 357, and 131 sources, respectively.

Finally, to reduce potential systematics in the stellar mass estimates, we removed from our sample any sources with $\geqslant 65\%$ flux contamination from neighboring objects[9] in either IRAC band. After this step, the sample included 523, 204, and, 65 objects at $z \sim 6$, 7, and 8 (corresponding to $\sim 66\%$, 57%, and 50% of the parent sample), respectively. In Figure 3, we present our final sample in terms of the UV luminosity, with

sources segregated by the significance of the associated IRAC measurements. This figure and Table 2 indicate that, for the $z \sim 6$–8 samples, $\sim 25\%$ of sources remain undetected (at 2σ) in at least one of the IRAC bands. To account for this selection in our SMF estimates, we implemented the Monte Carlo simulation described in Appendix A. The estimated statistical corrections allow us to recover the UV luminosity function (LF) over the full range of absolute magnitudes, indicating that we can confidently measure the corresponding SMFs (see Figure 14 of the Appendix). However, the median of the corrections become very large (>10×) for $M_{UV} \gtrsim -16.75$, -17.25, and ~ -17.5 mag at $z \sim 6$, 7, and ~ 8, respectively, making the associated volume densities more uncertain. For this reason, in our analysis we flag those measurements that are affected by very large corrections.

2.2. Sample at $z \sim 9$

The initial $z \sim 9$ sample included the YJ-dropouts from Oesch et al. (2014), Bouwens et al. (2016b), and Bouwens et al. (2019) identified over the five CANDELS fields and are summarized in Table 2 of Bouwens et al. (2019). For consistency with the $z \sim 6$–8 selection criteria, we excluded GS-z9-5 and UDS910-5 because their probability of being genuine $z > 8$ sources, $p(z > 8) \sim 0.55$ and 0.58, respectively, does not satisfy our threshold ($p(z > 8) = 0.6$). We complemented this sample with GN-z10-3 from Oesch et al. (2014), which has a photometric redshift of $z_{phot} = 9.5$, and 6 sources identified by Oesch et al. (2013) over the XDF region (we excluded XDFyj-39446317 due to uncertainties on its high-z nature; see Oesch et al. 2013 for details). This resulted in a total of 19 sources. Given the availability of updated, deeper IRAC 3.6 μm and 4.5 μm mosaics from GREATS, we measured new flux densities in those bands for all sources in the GOODS fields using the same procedures described in the previous section. These new IRAC flux densities were used in combination with the existing HST measurements to confirm that the $z \sim 9$ candidates included in our sample are indeed at $z \sim 9$. No update was made to the estimated photometric redshifts of the $z \sim 9$ candidates we included to maintain consistency with volume density estimates from published

---

[9] We define the contamination c to be $c = \sum f_n / (f_s + \sum f_n)$, where f_s is the flux density estimated for the source in a $1\overset{''}{.}8$-diameter aperture, and $\sum f_n$ is the cumulative flux density from all neighboring sources entering that aperture.
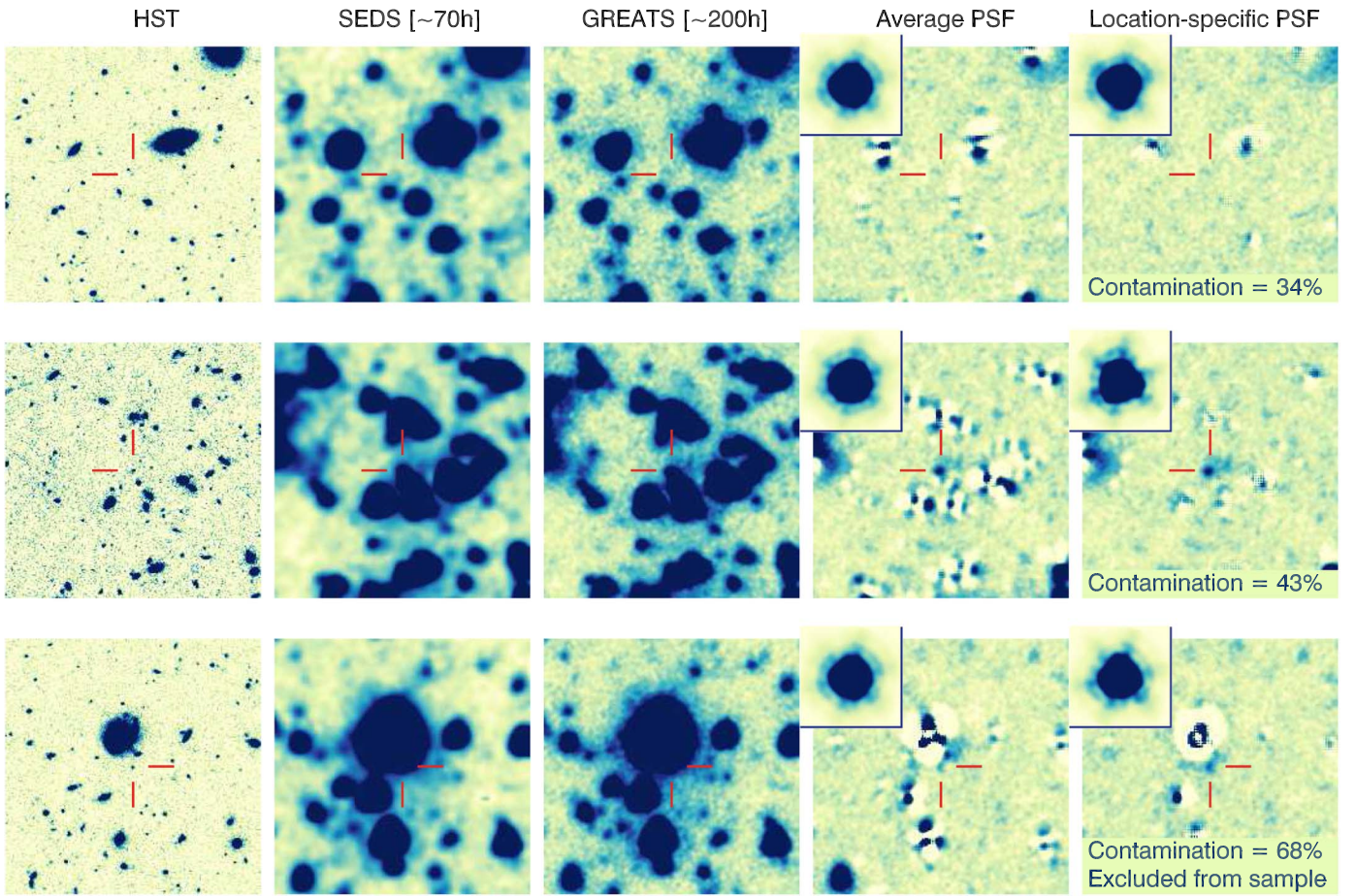
Figure 2. Illustration of our sophisticated procedures for handling the deep IRAC data used in this work. Each row refers to a specific object in the $z \sim 7$–8 compilation of Bouwens et al. (2015), which constitutes our initial sample (from top to bottom, GSDZ-2460945596, GNWZ-7268117400, and GSDZ-2288549126). Each stamp is $\sim 30''$ per side and, in each row, they match to the same region of sky. In each stamp, the location of the high-z source corresponds to the intersection of the two red segments. From left to right, columns present the combined image from HST ($J_{125} + JH_{140} + H_{160}$), an image stamp at 3.6 μm from SEDS (Ashby et al. 2013), which corresponds to a nominal coverage depth of ~ 70 hr (including also the GOODS IRAC data), and the same region in the 200 hr GREATS 3.6 μm mosaic. In the last two columns, we present our results subtracting neighboring sources with MOPHONGO adopting, first, an average PSF and, second, the specific PSF reconstructed at the location of the source, accounting for the orientations of all contributing observations (as first pioneered in Labbé et al. 2015). The estimated contamination from neighboring sources is reported at the bottom of the rightmost panel. All IRAC stamps share the same flux density cuts. The adopted PSF is shown in the top left corner of the corresponding stamp. As can clearly be seen in the rightmost column, the combination of increased depth and accurate PSF reconstruction from the location-specific PSF allow us to obtain more robust flux densities in the IRAC bands. The last row shows an object excluded from our final sample because of the large contamination (>65%) from the very bright neighboring source, which made photometry more uncertain, even though the removal of the neighbors was reasonably successful.

studies. We defer the discussion on the improved photometric redshifts for the $z \sim 9$ sample to a future work.

2.3. Sample at z ~ 10

For the $z \sim 10$ sample, we adopted the compilation of Oesch et al. (2018), which includes sources identified over the GOODS-N, GOODS-S, and XDF fields. We complemented this sample with one additional J-dropout identified in the XDF field by Bouwens et al. (2015, XDFJ-4023680031), for a total of six sources. For all sources, we measured new 3.6 μm and 4.5 μm flux densities from GREATS using the same methods described in Section 2. Similarly to the procedure we adopted for the $z \sim 9$ sample, we used the new IRAC measurements to further validate the sources in our sample as bona fide $z \sim 10$ galaxies but adopted the redshifts previously reported in the literature for our stellar mass estimates.

3. Stellar Mass Estimates

In this section, we present the general framework adopted for estimating the stellar masses of the galaxies in our $z = 6$–10 samples. The procedure we utilize for galaxies in our $z = 6$–8 samples depends on whether we detect individual sources (at 2σ level or above) or not, to limit the impact of potential systematics. The two approaches are described in Sections 3.2 (IRAC-detected sources) and 3.3 (IRAC non-detected sources; but see, e.g., Furtak et al. 2021 for a different approach for measuring stellar masses of galaxies with marginal IRAC detections). Furthermore, because the 3.6 μm band probes the rest-UV for $z \gtrsim 9$, we implemented different procedures for the $z \sim 9$ and $z \sim 10$ samples, which we present in Sections 3.4 and 3.5, respectively. In Figure 4, we present a flowchart to better understand the specific procedures adopted to compute the stellar mass of the sources in our samples, depending on the
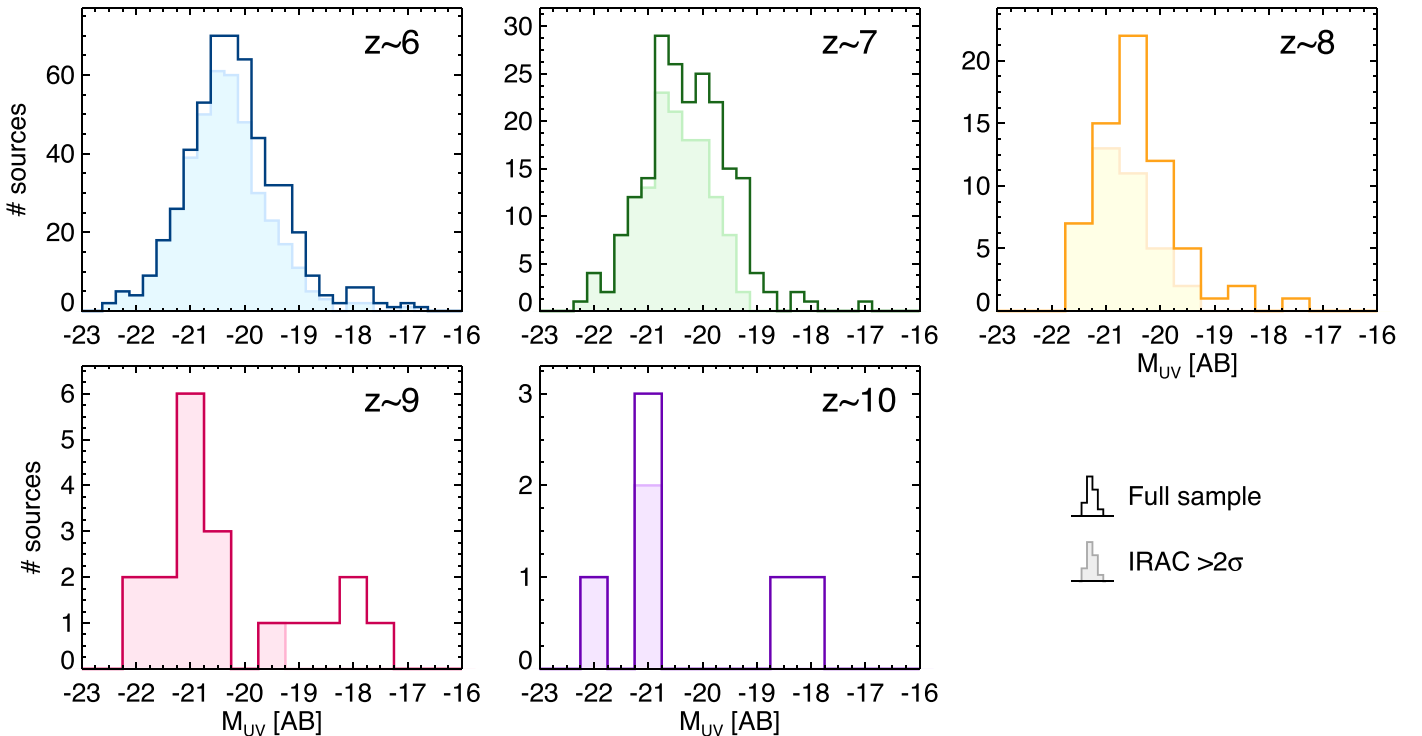
Figure 3. UV luminosity distribution of the sources in our samples after removing objects with potentially high contamination from neighbors in each of the IRAC bands. The corresponding redshift bin for each panel is shown in the top right corner. In each panel, the histogram marked by the darker line corresponds to the full sample, while the filled histogram corresponds to those sources with S/N > 2 in both the IRAC bands ($z \sim 6$, 7, and 8) or in the 4.5 μm band only ($z \sim 9$ and 10).

redshift and significance of the IRAC detections for each individual source.

3.1. Modeling Assumptions

For our stellar population parameter estimates we considered the Bruzual & Charlot (2003) composite stellar population models with a Salpeter IMF (1955) between $0.1\mathcal{M}_\odot$ and $100\mathcal{M}_\odot$, and with a slope -2.35, a $0.2Z_\odot$ metallicity, and a constant star formation history with a minimum age of 10^6 yr and a maximum age set by the age of the universe at each specific redshift. Template fitting was performed with FAST (Kriek et al. 2009), fixing the redshift of each source to the value produced by EAZY. In our fits, we consider a dust attenuation in the range $A_V = 0$–3 mag with a Calzetti et al. (2000) curve, assuming the same dust law for both the stellar continuum and the nebular emission.

Numerous studies suggest that the SEDs of galaxies observed at early epochs are characterized by strong nebular line emission (e.g., Schaerer & de Barros 2010; Labbé et al. 2013; Stark et al. 2013; Smit et al. 2014; Faisst et al. 2016; De Barros et al. 2019; Faisst et al. 2019, 2020; Endsley et al. 2021), with typical equivalent widths EW(Hα) and EW([O III] +Hβ) in excess of few $\times$ 100 Å–$\sim$1000 Å. Furthermore, photoionization models predict that emission by nebular continuum could significantly contribute to the observed flux densities of young stellar populations even when they are probed through broadband filters (e.g., Zackrisson et al. 2008, 2011; Schaerer & de Barros 2010; Inoue 2011).

We accounted for the contribution of nebular emission, both lines and continuum, processing the SED templates with CLOUDY version 17.02 (Ferland et al. 2017). For simplicity, we assumed a spherical constant-density nebula with $n(H) = 100 \, \mathrm{cm}^{-3}$, a gas metallicity matching that of the stellar

component ($0.2Z_\odot$), an ionization parameter $\log U = -2.5$, consistent with recent work (e.g., Stark et al. 2017; De Barros et al. 2019), and that the escape fraction was negligible.

We also implemented a second set of SED templates, where we added to the Bruzual & Charlot (2003) templates only the effects of nebular continuum, ignoring any contribution from nebular line emission. This new set of SED templates was used in estimating stellar masses for those objects undetected in IRAC bands and sources at $z \sim 9$ and $z \sim 10$ after updating their IRAC flux densities using the phenomenologically motivated relations described in Sections 3.3–3.5. An increasing number of studies indicate that the red IRAC colors observed for individual sources at $z \sim 7$–8 could result from evolved stellar populations (e.g., Hashimoto et al. 2018; Strait et al. 2020; Roberts-Borsani et al. 2020). However, the observations unambiguously supporting such an interpretation regard just a few sources. The nebular line emission interpretation is supported by a recent study showing that on average $z \sim 7$–8 Lyman-break galaxies (LBGs) have UV–optical colors consistent with no significant Balmer break (Stefanon et al. 2021a). Such Balmer-break sources therefore would not appear to have a large impact on the conclusions we draw regarding the mass for statistical samples of $z \sim 6$–8 galaxies. For these reasons, we only consider the color excess to be the result of contributions from nebular lines.

3.2. Stellar Mass Estimates for Sources Detected by IRAC at $z \sim 6$, $z \sim 7$, and $z \sim 8$

For the those sources in our $z \sim 6$, 7, and 8 samples with $\geqslant 2\sigma$ detections in both IRAC 3.6 μm and 4.5 μm bands, i.e., the majority of sources in these samples ($\sim$75%—see e.g., Figure 3), we computed the stellar masses by running FAST with the Bruzual & Charlot (2003) template set enriched with
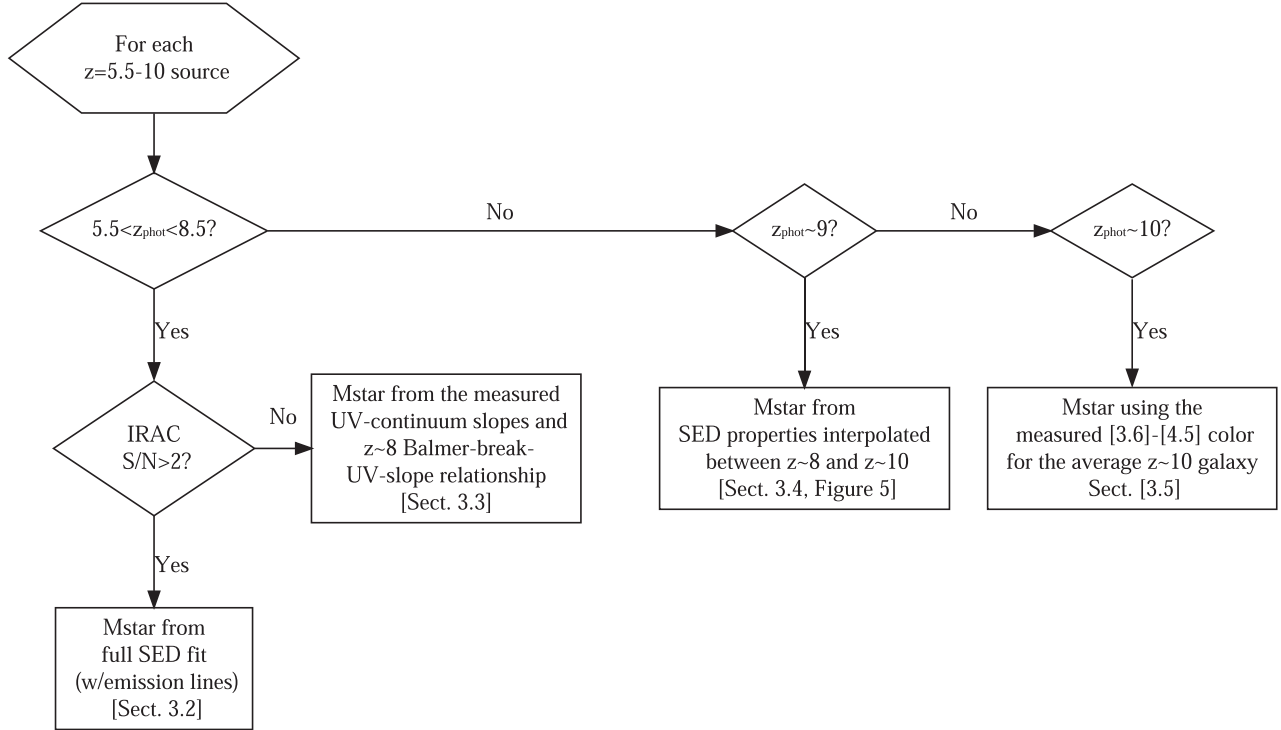
Stellar mass estimate flowchart

Figure 4. Flowchart summarizing the different procedures followed to estimate the total stellar mass $\mathcal{M}_\star$ of galaxies in our sample depending on the source redshift and the significance of the IRAC detections.

nebular continuum and emission line information from CLOUDY, obtained as described in Section 3.1, and shown in Figure 4.

3.3. Stellar Mass Estimates for Sources Undetected by IRAC at z ~ 6, z ~ 7, and z ~ 8

Estimates of $\mathcal{M}_\star$ for the small fraction ($\sim$25%) of galaxies in our sample that are not detected by IRAC are going to be quite uncertain by comparison. Fortunately, we can make use of an observational correlation between the UV-continuum slope β and the amplitude of the Balmer break that has been reported by both Oesch et al. (2013) and Stefanon et al. (2021a). This correlation then provides a good proxy for the age of the stellar population.

Using both individual and stacked $z_{\mathrm{phot}} = 7.3$–8.7 sources, Stefanon et al. (2021a) showed that there is a clear correlation between the UV-continuum slope β, that is determined using the J and H measurements, and the Balmer break amplitude. For the sources with the bluest UV slopes ($\beta \sim -2.5$), Stefanon et al. (2021a) find blue ($H - [3.6] \sim -0.5$ mag) colors, and the $H - [3.6]$ colors become increasingly red as one moves to redder UV-continuum slopes $\beta \sim -1.6$ (see their Figure 5). Because at these redshifts the 3.6 μm band probes rest-frame wavelengths just redward of the Balmer break, while the H band probes the rest-frame UV, the above trend suggests that the UV slope could be used as a proxy for the break amplitude, and hence for the age of a stellar population. Oesch et al. (2013) found a very similar correlation between the amplitude of the Balmer break $H - [4.5]$ and the UV-continuum slope β for $z \sim 4$ galaxies.

To estimate the new 3.6 μm flux densities, we therefore adopted the relationship between β and the $H - [3.6]$ color found by Stefanon et al. (2021a) for $z \sim 8$ LBGs, after correcting it for the effects (0.2 mag) of [O II] emission contaminating the 3.6 μm band at $z \sim 8$ (see Stefanon et al. 2021a for more details):

$$H - [3.6] = 0.03 + 1.78(\beta + 2.2). \quad (1)$$

This relationship was derived for galaxies with UV-continuum slopes β ranging from -2.6 to -1.9. We adopted a constant value of $H - [3.6] = 0.56$ mag when $\beta > -1.9$. The corresponding 4.5 μm flux densities were computed assuming the rest-frame optical had a flat f_ν SED. A flat f_ν SED is expected from stacking analysis of observations at similar redshifts (e.g., González et al. 2012; Stefanon et al. 2017), and it is predicted by photoionization modeling as the effect of nebular continuum emission in relatively young stellar populations of star-forming galaxies (e.g., Schaerer & de Barros 2009). The flat SED hypothesis is also consistent with the negligible dust content found for $\mathcal{M}_\star \lesssim \mathcal{M}_\star^*$ galaxies at high redshifts (e.g., Bouwens et al. 2020).

Our hypothesis of a flat SED at rest-frame optical wavelengths for $z \sim 6$–8 is consistent with observations only if we assume a negligible contribution of nebular lines in the 4.5 μm band. Later in this section, we describe how we accounted for this in our SED fitting. Following Stefanon et al. (2021a), we computed the UV slope β from the best-fitting SED template of each individual source.

Having established the described correlation, the challenge became applying it to galaxies distributed over the redshift range $z \sim 6$–8, requiring that we account for the different rest-frame wavelengths of the H_{160} and 3.6 μm filters. To deal with
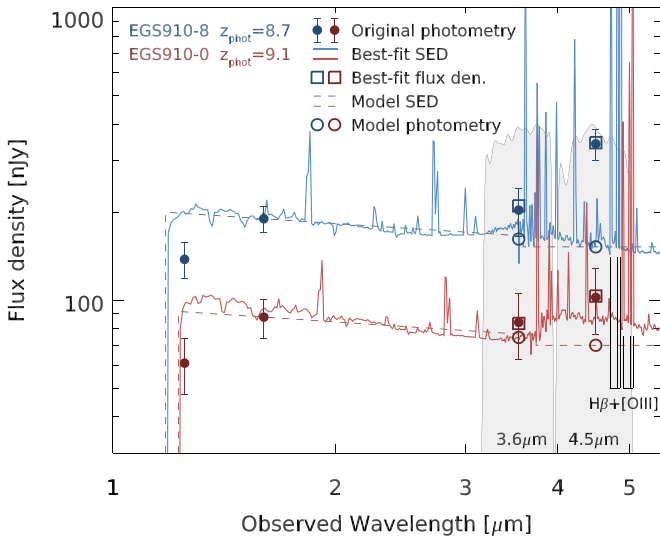
Figure 5. Illustration of the challenges we face in estimating the stellar masses of $z \sim 9$ sources, given the uncertain position of the Balmer break/jump and [O III]+Hβ emission lines relative to the 3.6 μm and 4.5 μm bands and of the procedure we adopted to reduce the associated systematic effects. Presented are two distinct sources in the upper and lower halves of the redshift range of our $z \sim 9$ sample (EGS910-8 at $z_{\rm phot} \sim 8.7$, and EGS910-0 at $z_{\rm phot} \sim 9.1$—Bouwens et al. 2019—blue and red, respectively). All flux densities of EGS910-0 were arbitrarily rescaled by a factor 0.7 to improve readability. The original photometric measurements are marked with filled circles, while the corresponding best-fit templates are presented as solid curves; the flux densities in the 3.6 μm and 4.5 μm bands for the best-fit templates are indicated as open squares. The two sets of vertical lines close to the bottom right corner indicate the location of Hβ and of the [O III] doublet at the redshifts of the two galaxies. The two filled gray regions correspond to the transmission curves of the IRAC 3.6 μm and 4.5 μm bands, arbitrarily renormalized. The typical photometric redshift uncertainties ($\Delta z \sim 0.6$–0.8) do not allow us to properly estimate the relative contribution of the rest-frame optical light to the observed flux density in the 3.6 μm band, and of some among the strongest emission lines (Hβ and [O III]) to the flux densities in the 4.5 μm band. These are necessary to constrain the amplitude of the Balmer break and therefore the age of the stellar population. For each source, we therefore created a model SED (dashed curves), free from nebular lines contribution, interpolating the empirical relationships we derived from observations of $z \sim 8$ and $z \sim 10$ galaxies (see main text), and computed the expected flux densities in the IRAC 3.6 μm and 4.5 μm bands (open circles). We combined the new model photometry with the existing HST measurements to estimate the stellar masses through a new SED fit (see Section 3.4).

this aspect, we updated the newly computed $H - [3.6]$ color of each source assuming a flat f_ν SED at rest-frame optical wavelengths and a power law with slope β in the rest-UV. In doing so, we retained the same uncertainties for the IRAC flux measurements as originally estimated by MOPHONGO. The flux densities free of emission lines that we obtained from the above procedure were then used to derive our stellar mass measurements for those objects with S/N < 2 in either one of the 3.6 μm or 4.5 μm bands. For this step, we ran FAST using the emission-line-free template set.

To test the robustness of the stellar mass measurements for the IRAC-undetected sources, we also computed the stellar mass of sources with $>2\sigma$ detection in both IRAC bands after replacing the IRAC flux densities with those obtained from Equation (1) and assuming $[4.5] = [3.6]$. In comparing the stellar mass estimates made in these two separate ways, we recovered essentially identical results, validating this method. These tests show that we can confidently use this method for computing the stellar masses for $z \sim 6$, 7, and 8 galaxies

detected at $<2\sigma$ significance with IRAC (see Appendix B for further details).

3.4. Stellar Mass Estimates for the $z \sim 9$ Sample

The approaches used in Sections 3.2 and 3.3 cannot be applied at $z \gtrsim 9$. There are two limiting factors. First, complications arise from the Balmer break beginning to move into and through the IRAC 3.6 μm band at $z \sim 9$, and second, it becomes more challenging to determine β from the HST WFC3 IR bands. More details on the challenges of working with $z \sim 9$ galaxies are discussed below, while in Figure 5 we present the application of our procedure to two of the sources in our $z \sim 9$ sample.

First, the uncertainties in photometric redshifts (typical values of $\Delta z \sim 0.6$–0.8) do not lead to clarity in the relative contribution from rest-frame UV (blueward of the Balmer break) and rest-frame optical light (redward of the Balmer break) to the IRAC 3.6 μm band (ranging from $\sim 50\%$ optical light contribution at $z \sim 8.7$ to $\lesssim 10\%$ at $z \sim 9.3$). Furthermore, the Hβ and [O III] emission lines can significantly contribute to the flux density in the 4.5 μm band up to $z \sim 9.3$, potentially mimicking the existence of more evolved stellar populations. This makes for an uncertain SED fit, limits insight into the break amplitude, and thereby increases the uncertainty in stellar ages and, consequently, stellar masses. Second, only the JH_{140} and H_{160} bands are available to probe the UV-continuum slopes for $z \sim 9$ galaxies (e.g., Dunlop et al. 2013; Bouwens et al. 2014a). The wavelength coverage of this latter band substantially overlaps with that of H_{160}, limiting the wavelength leverage for the UV slope estimates, while its extension to the blue makes JH_{140} sensitive to the intrusion of the Lyman break at $z \sim 9$, limiting its utility for measuring β.

To overcome, at least in part, these challenges, we did not adopt the original IRAC photometry in our SED fitting, but instead we estimated the separate contributions above and below the Balmer break of the rest-frame UV and of the rest-frame optical light to the 3.6 μm band using the procedure described below.

Supported by the consistent correlations found between the UV luminosity and the UV slopes β for LBGs at $z > 4$ (e.g., Finkelstein et al. 2012; Bouwens et al. 2014b; Rogers et al. 2014; Bhatawdekar & Conselice 2021), we computed the contribution to the 3.6 μm band from the rest-frame UV light assuming each source had a power-law-like SED with slope β equal to the median of the UV slopes of $z \sim 8$ galaxies in our sample with similar UV luminosity ($|\Delta M_{\rm UV}| \leqslant 0.5$ mag).

The contribution from the rest-frame optical was then obtained by interpolating between the $z \sim 8$ $H_{160} - [3.6]$–β relation (Equation (1)) and the $H_{160} - [4.5]$ color at $z \sim 10$ (see Section 3.5) using the same median UV slopes adopted for the rest-UV light estimates.

These two contributions were ultimately combined, weighting by the corresponding fraction of the 3.6 μm-band coverage given the individual photometric redshifts. We also verified that $\sim 94\%$ of the newly computed flux densities in the 3.6 μm band were consistent at $<2.4\sigma$ with the original measurements, increasing the confidence on our procedure. The emission line-free flux density in the 4.5 μm band was then computed assuming the rest-frame optical has a flat f_ν SED. Stellar masses were finally obtained running FAST on these reconstructed

Table 3
$M_{\rm UV}$ vs. $\mathcal{M}_\star$ Linear Fit Parameters

Redshift bin	$\log \mathcal{M}_\star/\mathcal{M}_\odot$ for $M_{\rm UV} = -20.5$	Slope	$\mathcal{M}_\star/L_{\rm UV}$[a] $[\mathcal{M}_\odot/L_\odot]$
6	9.0 ± 0.1	-0.57 ± 0.02	$0.027^{+0.002}_{-0.002}$
7	8.9 ± 0.1	-0.49 ± 0.08	$0.024^{+0.004}_{-0.003}$
8	8.8 ± 0.1	-0.49 ± 0.12	$0.020^{+0.006}_{-0.005}$
9	8.6 ± 0.1	-0.46 ± 0.03	$0.012^{+0.001}_{-0.001}$
10	8.5 ± 0.1	-0.41 ± 0.02	$0.010^{+0.001}_{-0.001}$

Note.
[a] Stellar mass-to-light ratio computed from the stellar mass for $M_{\rm UV} = -20.5$ mag.

SEDs, adopting for consistency the SED template set where the emission lines have been explicitly removed.

Our $z \sim 9$ sample includes one galaxy spectroscopically confirmed at $z_{\rm spec} = 8.683$ (EGS910-10; Roberts-Borsani et al. 2016). The spectroscopic redshift enables the unambiguous recovery of the contribution of the rest-frame optical light to the IRAC 3.6 μm band. An SED fit performed with the original photometry on the same template set adopted in Section 3.2 results in a stellar mass lower by only 0.05 dex than the value we obtained applying the procedure described above, increasing our confidence on the results. Finally, the median $H_{160} - [3.6]$ color for the sources in our $z \sim 9$ sample is 0.07 mag. This value is consistent with the -0.03 ± 0.14 found at $z \sim 8$ by Stefanon et al. (2021a), which is indicative of young stellar population ages, and supports the low $\mathcal{M}_\star/L_{\rm UV}$ values we find (see, e.g., Table 3).

3.5. Stellar Mass Estimates for the $z \sim 10$ Sample

As we noted above, for $z > 9$, the Spitzer/IRAC 3.6 μm band begins to move blueward of the Balmer break suggesting it could be effectively used for a UV-slope measurement. However, despite the unprecedented depth provided by the GREATS mosaics, only 3/6 of our $z \sim 10$ candidates have $>2\sigma$ detections in the 3.6 μm band. For these reasons, before computing the stellar masses, and to guide the fitting, we updated the 3.6 μm and 4.5 μm flux densities of all sources with values corresponding to a flat SED, i.e., $H_{160} - [3.6] = 0.0$ mag and blue $H_{160} - [4.5] = -0.13$ mag colors. These colors are consistent with the stacking analysis performed with the same sample of $z \sim 10$ sources done by Stefanon et al. (2021, in preparation); moreover, an approximately flat UV slope at $z \sim 10$ has been reported by Wilkins et al. (2016) and, for $M_{\rm UV} \sim -21$ mag sources at $z \sim 9$, by Bhatawdekar & Conselice (2021). We reduced the [4.5] flux density by 0.2 mag to remove the estimated [O II] contribution, resulting in an adopted $H_{160} - [4.5]$ color of -0.33 mag for all sources. In the process, we maintained the same flux density uncertainties originally measured in the 3.6 μm and 4.5 μm bands. We verified that the 3.6 μm flux densities of all sources computed in this way were consistent at $\sim 2\sigma$ with the original measurements. This approach is consistent with computing the individual $\mathcal{M}_\star$ assuming all sources possess the same $\mathcal{M}_\star/L_{\rm UV}$ ratio, as derived from the stack of the $z \sim 10$ sample.

4. Stellar Mass and IRAC Measurements in the $\mathcal{M}_\star - M_{\rm UV}$ Plane

To provide essential context for the depth to which we can robustly probe the galaxy SMFs at $z \geqslant 6$ with existing Spitzer/ IRAC data sets, it is useful to examine the stellar mass and IRAC measurements we derived for our $z = 6-10$ samples in the stellar mass ($\mathcal{M}_\star$) versus the absolute UV magnitude ($M_{\rm UV}$) plane. We present this in Figure 6. We indicate with open circles those sources with a $<2\sigma$ detection significance in either one of the IRAC bands for the $z \sim 6, 7, 8$ samples, or just in the 4.5 μm band for the $z \sim 9$ and $z \sim 10$ samples, providing an indication of the fraction of sources with higher or lower quality constraints on the estimated stellar masses. The panels show an overall correlation between $\mathcal{M}_\star$ and $M_{\rm UV}$ at all redshifts, even though the scatter in $\mathcal{M}_\star$ can be as large as $\gtrsim 1.5$ dex for specific $M_{\rm UV}$ values. Large scatter is predicted by some simulations, as the result of a real variation in the specific SFR (e.g., Ceverino et al. 2018), but a detailed study of the mass-to-light ratios $\mathcal{M}_\star/L_{\rm UV}$ at these redshifts, while interesting, is beyond the scope of this work.

For illustrative purposes, in Figure 6 we present a simple linear fit to the median values of the stellar masses in bins of $M_{\rm UV}$. In particular for this analysis, no statistical correction is made to account for our initial removal of sources with contamination by neighbors in the IRAC bands. The results of the fit are marked by colored lines in Figure 6 and are listed in Table 3. In fitting the linear relation at $z \sim 8, 9$, and 10, we included measurements to $M_{\rm UV} \sim -18.5$, -19.2, and -18 mag, respectively, dominated by sources individually undetected in the available IRAC data (open circles in Figure 6), to provide sufficient leverage to better constrain the fit results. While this adds some arbitrariness to the slope estimates, we judged that the linear fit would otherwise provide a worse representation of the individual measurements. The slopes are consistent with a constant value of ~ -0.55 across the $z \sim 6-8$ redshift range, and of ~ -0.45 at $z \sim 9$ and ~ 10.

In Appendix C and Figure 16 of Appendix C, we include more detailed comparisons between our $\mathcal{M}_\star - M_{\rm UV}$ relation and previous work. Here, we note that our slope estimates are in general consistent with previous determinations at similar redshifts (e.g., Duncan et al. 2014; Song et al. 2016; Bhatawdekar et al. 2019; Kikuchihara et al. 2020), while the intercept we have derived is lower on average by $\sim 0.2-0.3$ dex (see Figure 16 in Appendix C). While the observed differences are not especially surprising and consistent with the range of scatter seen in the literature, we emphasize that our very deep IRAC photometry should provide the most accurate constraints for the stellar population properties of galaxies achieved thus far at $z \sim 6-10$.

As expected, most of the sources at the faint, and typically low-mass, end only have marginal IRAC detections. The fraction of sources with an IRAC-detection significance in excess of 2σ is presented in the panels to the right of each $\mathcal{M}_\star - M_{\rm UV}$ plot, where the error bars reflect the Poissonian uncertainties. To represent analytically the dependence of the IRAC detection fraction on stellar mass, we fit the following form of the Gompertz function to the observed fraction:

$$f(\mathcal{M}_\star) = \exp[-m_0 \exp(-a_0 \mathcal{M}_\star)] \qquad (2)$$

where a_0 controls the steepness of the decrease in counts, while m_0 applies a rigid shift in stellar mass to the curve. The
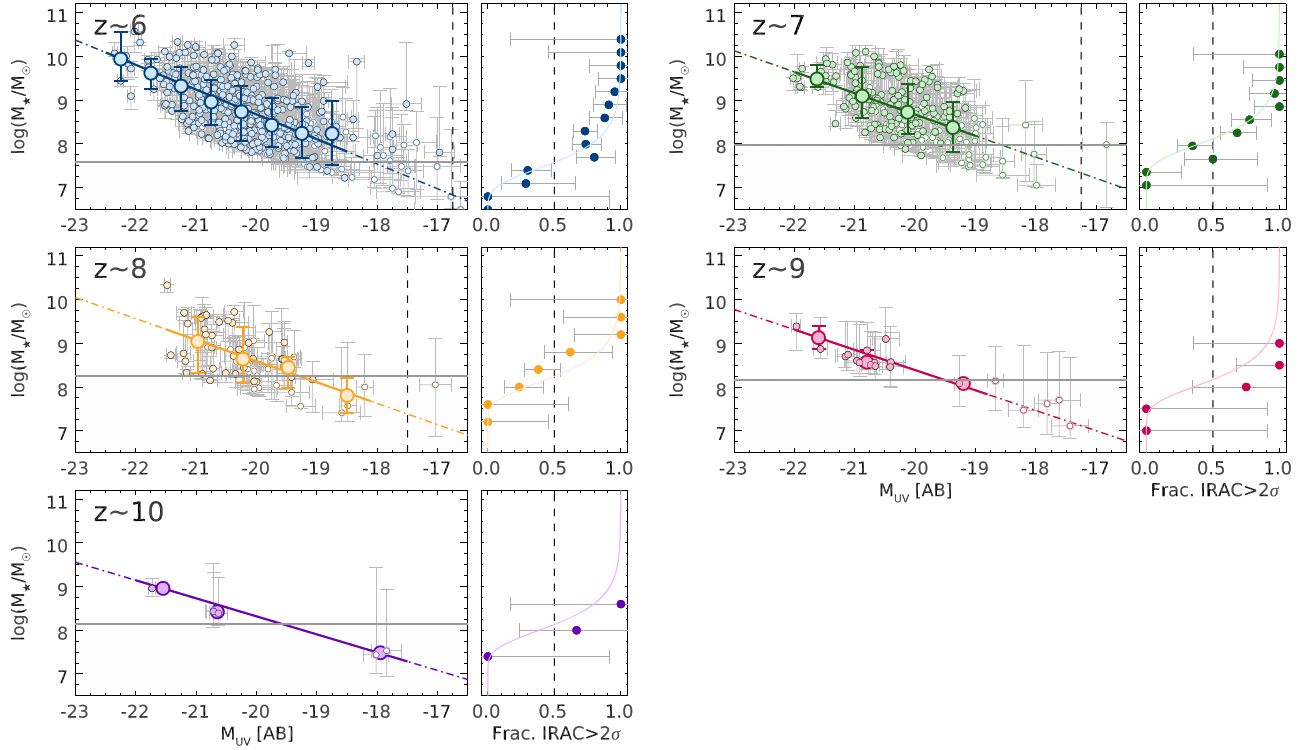
Figure 6. For each redshift bin, indicated at the top left corner of the larger panels, we present a set of two plots. In the right-hand plot, we present the fraction of galaxies with 3.6 μm and 4.5 μm flux densities detected at 2σ level or better (4.5 μm only for the z ∼ 10 sample), in bins of stellar mass (colored points and error bars —note the unusual plot orientation—rotated by 90°). The vertical dashed lines mark the 0.5 fraction we adopted as our criterion to identify the lowest stellar mass that can confidently be used in the measurement of the stellar mass function, while the colored solid curves mark the best-fitting Gompertz function (see text). The plot on the left side of each panel shows the individual sources we selected in each redshift bin in the $M_{UV} - \mathcal{M}_\star$ plane (open and filled small circles). Filled circles mark those sources detected at the 2σ level or better in both the 3.6 μm and 4.5 μm bands, while the small open circles correspond to sources with S/N < 2σ in at least one of the two IRAC bands. The large filled circles with error bars correspond to the median and 68% confidence intervals on the stellar masses in varying-width bins of UV luminosity. The colored solid lines indicate the best-fit linear relation through the median estimates, while the dotted–dashed lines represents its extrapolation to brighter and fainter luminosities. For the z ∼ 8, 9, and 10 redshift bins, we also included median estimates for M_{UV} bins dominated by sources with <2σ in either IRAC band to better guide the fits. The vertical black dashed line marks the faintest UV luminosity down to which we can reliably recover the z ∼ 6–8 UV LF after removing sources with contaminated IRAC measurements (see Figure 14); they are absent for the z ∼ 9 and z ∼ 10 bins because for these samples we did not apply any cleaning. The hatched gray region identifies the range in stellar mass where the fraction of sources with >2σ in both IRAC bands is smaller than 0.5. The sources selected for our SMF estimates have robust stellar mass estimates down to the applied limits; sample cleaning does not systematically affect the recovery of the volume densities down to $\mathcal{M}_\star \sim 10^8 \mathcal{M}_\odot$ across the full range of redshifts considered here.

Gompertz function is a generalization of the logistic function, and it allows to approach the two asymptotes with different bendings (i.e., its shape is asymmetric). This represents our measurements well. During the fit of the fractions for $z \geqslant 7$, we only left m_0 free to vary, fixing a_0 to the value obtained at $z \sim 6$ ($a_0 \equiv 2.4$). Note that fitting for both parameters at $z \sim 7$ produced a value of a_0 very similar to that of $z \sim 6$, although with larger uncertainties. The fit results are shown with the black lines in the right-hand panels of Figure 6.

5. Completeness and Selection Biases

Another important part of deriving galaxy SMFs is an understanding of the selection volumes available from our samples for sources as a function of their stellar mass. Our sample selection relies on Lyman-break criteria, which, by construction, are biased against evolved, redder systems, more likely included in selections exclusively based on photometric redshift criteria (see also Fontana et al. 2006; Duncan et al. 2014; Grazian et al. 2015; Song et al. 2016; Stefanon et al. 2017). Stefanon et al. (2017) showed that at $z \sim 4$ the LBG criteria are able to recover at least ∼75% of the sources from photometric redshift selections for stellar masses

$\mathcal{M}_\star \lesssim 10^{10} M_\odot$ and concluded that use of LBG criteria to select their $z \sim 4$ sample did not produce especially different results than use of photometric redshift criteria. Because we expect that the fraction of evolved systems at $z > 4$ is even lower than at $z \sim 4$, we expect there is effectively little difference between the LBG selections we use at $z > 4$ relative to similar selections constructed using photometric redshift criteria.

Interestingly, an increasing number of studies are revealing the existence of extremely red, massive objects with $\mathcal{M}_\star \gtrsim 10^{10.5} \mathcal{M}_\odot$ at $z > 3 - 4$ (see, e.g., Yan et al. 2004; Huang et al. 2011; Caputi et al. 2012, 2015; Stefanon et al. 2015; Wang et al. 2016, 2019; Alcalde Pampliega et al. 2019; Williams et al. 2019; Fudamoto et al. 2020; Gruppioni et al. 2020; Romano et al. 2020; Talia et al. 2021). Most of these would remain hidden at higher redshifts, even at the near-IR wavelengths usually adopted for the detection of high-redshift sources in deep extragalactic fields. However, the limited samples and poor knowledge of their physical properties make estimating their contribution to the stellar mass budget at higher redshifts highly uncertain. Nonetheless, we expect, as noted above, that their integral contribution to the SMF will be small, even if they may contribute more at the highest masses. Furthermore, analyses of the deepest ALMA observations in

the Hubble UDF (HUDF) field have found no indication of dusty sources at $z > 4$ (e.g., Bouwens et al. 2016a, 2020; Dunlop et al. 2017), in particular at low stellar masses.

These results indicate that the completeness in stellar mass of our samples is not significantly affected by the LBG criteria adopted for their selection. In particular, our samples can be considered complete in stellar mass down to the limits in UV luminosity, once the detection efficiency and the selection we applied to the IRAC flux densities are taken into account.

While the selection efficiencies of our LBG samples are statistically accounted for in our volume estimates (see Bouwens et al. 2015), we use a separate procedure, discussed in Section 2 and Appendix A, to include the impact of the quality cuts we applied to the IRAC flux densities on the completeness of our samples. In the following, we further discuss issues that limit our ability to robustly recover the SMFs down to the lowest stellar masses seen in our UV selections.

We consider our SMFs to be robustly determined down to stellar masses for which the fraction f of $>2\sigma$ detections in both IRAC bands is larger than 50% (i.e., $f(\mathcal{M}_\star) \geqslant 0.5$), as discussed in Section 4 (see Figure 6). With this 0.5 limit, inverting the Gompertz functions results in lower bounds of $\log(\mathcal{M}_\star/\mathcal{M}_\odot) = 7.6, 8.0, 8.2, 8.2$ and 8.1 at $z \sim 6, 7, 8, 9$, and $z \sim 10$, respectively.

Because of the correlation between the UV luminosity and stellar mass, one may expect that our ability to reconstruct the UV LF only to absolute magnitudes ~ 1–2 mag brighter than the detection limits (see our discussion in Section 2 and Appendix A) could systematically affect our measurements of the SMF by excluding otherwise legitimate sources. However, Figure 6 shows that the limits in UV luminosity that we find do not impact the stellar mass completeness of our $z \sim 6$ samples and only very marginally impact those at $z \sim 7$ and $z \sim 8$, where the selection in UV luminosity excludes just two sources close to our stellar mass threshold. Since their stellar mass is constrained to only within ~ 1 dex, their value for our sample is minimal. Overall, these results increase our confidence in the sample selection and SMF measurements.

A more quantitative assessment of the potential bias against dusty and/or evolved systems in current rest-UV-selected samples requires selections at rest-frame optical wavelengths (e,g., Stefanon et al. 2015). This will only become possible at the redshifts considered in this study through forthcoming James Webb Space Telescope (JWST) programs such as PRIMER (Dunlop et al. 2021), COSMOS-Webb (Kartaltepe et al. 2021), UNCOVER (Labbe et al. 2021), PANORAMIC (Williams et al. 2021b), the UDF Medium Band Survey (Williams et al. 2021a), and WDEEP (Finkelstein et al. 2021).

While we have mentioned different approaches to sample selection, we note that the Lyman-break criteria we use constitute a set of well-defined color selections that can be modeled and univocally reproduced when accurate comparisons are needed. This ensures that the impact of selection biases on our derivation of galaxy characteristics is very well defined in general.

6. Results

6.1. The SMFs at z ∼ 6–10

We measured the SMF in bins of redshift centered at $z \sim 6$, 7, 8, 9, and 10, using the $V_{\max}$ estimator of Avni & Bahcall

(1980), which allows us to self-consistently combine samples selected from data of different depths. Briefly, based on Schmidt (1968), the volume density per unit stellar mass $\Phi(\mathcal{M}_\star)$ corresponding to the n_s sources with stellar masses within the interval $\Delta\mathcal{M}_\star$ centered at $\mathcal{M}_\star$ is given by:

$$\Phi(\mathcal{M}_\star) = \frac{1}{\Delta\mathcal{M}_\star} \sum_{i=1}^{n_s} \frac{1}{V_{\max,i}}. \quad (3)$$

In the analysis of Avni & Bahcall (1980), $V_{\max,i}$ is the effective comoving volume associated with each source i as given by:

$$V_{\max,i} = \sum_{j=1}^{n_f} V_{i,j} \quad (4)$$

where the sum runs over the n_f fields, and $V_{i,j}$ is the volume associated to source i assuming it was detected in field j.

We adopted the comoving volumes V_j of Bouwens et al. (2015), which already account for the effects of detection incompleteness, LBG selection, and photometric redshift scatter. Uncertainties were computed with the binomial approximation of Gehrels (1986), adding in quadrature cosmic variance from Moster et al. (2011), consistent with more recent determinations (e.g., Bhowmick et al. 2020), after rescaling it by the square root of the number of fields (e.g., Driver & Robotham 2010).

The resulting measurements are listed in Table 4 and presented in Figure 7. Remarkably, the volume density of galaxies with stellar mass $\log(\mathcal{M}_\star/\mathcal{M}_\odot) \sim 8.8$ increased by about three orders of magnitude in the ~ 500 Myr elapsed between $z \sim 10$ and $z \sim 6$, suggesting an extremely rapid growth of the total stellar mass in galaxies at such early epochs.

We used the $V_{\max}$ measurements to fit a Schechter (1976) functional form, whose expression for logarithmic stellar masses is:

$$\phi(m)dm = \ln(10)\phi^* 10^{(m-m^*)(1+\alpha)} \exp(-10^{(m-m^*)})dm \quad (5)$$

where $m = \log(\mathcal{M}_\star/\mathcal{M}_\odot)$, $m^* = \log(\mathcal{M}_\star^*/\mathcal{M}_\odot)$, with $\mathcal{M}_\star^*$ being the pivot mass between the power law and the exponential regimes, α corresponds to the slope at the low-mass end, and ϕ^* is the overall normalization factor. For the $z \sim 6, 7$ and $z \sim 8$ redshift bins we allowed all three parameters to vary, while for the $z \sim 9$ and $z \sim 10$ bins we kept the low-mass end slope α and characteristic mass $\mathcal{M}_\star^*$ fixed to $\alpha \equiv -2$ and $\log(\mathcal{M}_\star^*/\mathcal{M}_\odot) = 9.5$,[10] respectively. The resulting parameterizations are represented by solid curves in Figure 7, with the filled areas showing the 68% confidence regions on the three parameters obtained by Monte Carlo sampling the Schechter parameterizations. The values of the Schechter parameters and their 68% uncertainties are listed in Table 5, while Figure 8 presents the contours corresponding to the 68% and 95% confidence regions where $\Delta\chi^2 \leqslant 2.30$ and 6.18, respectively.

Unsurprisingly, the confidence intervals in Figure 8 show that there is a considerable range in $\phi^*, \mathcal{M}_\star^*$, and α values that reasonably represent the observed mass functions—which is a reflection of how covariant the Schechter parameters are. Fortunately, in the case of the evolution of the characteristic stellar mass and the number density normalization factor (featured in the central panel of Figure 8), the evolution is

----

[10] If we let $\mathcal{M}_\star^*$ vary in the $z \sim 9$ fit, we obtain $\mathcal{M}_\star^* = 10^{9.54} M_\odot$.

Table 4
$V_{\rm max}$ Determinations of the SMF

Redshift Bin	$\log(\mathcal{M}_\star/\mathcal{M}_\odot)$[a]	ϕ $[\times 10^{-4}\ {\rm dex}^{-1}\ {\rm Mpc}^{-3}]$
6	7.80 ± 0.20[b]	225^{+42}_{-37}[b]
	8.20 ± 0.20	159^{+23}_{-21}
	8.60 ± 0.20	$42.9^{+6.3}_{-5.9}$
	9.00 ± 0.20	$25.3^{+3.8}_{-3.5}$
	9.40 ± 0.20	$7.85^{+1.50}_{-1.40}$
	9.80 ± 0.20	$4.93^{+1.36}_{-1.21}$
	10.20 ± 0.20	$1.01^{+0.43}_{-0.35}$
	10.60 ± 0.20	$0.0601^{+0.1381}_{-0.0517}$
7	7.75 ± 0.25[b]	$71.7^{+23.7}_{-18.3}$[b]
	8.25 ± 0.25	$39.4^{+6.9}_{-6.3}$
	8.70 ± 0.20	$13.2^{+2.7}_{-2.4}$
	9.10 ± 0.20	$7.70^{+1.67}_{-1.49}$
	9.50 ± 0.20	$3.18^{+0.88}_{-0.78}$
	9.90 ± 0.20	$1.68^{+0.63}_{-0.53}$
	10.30 ± 0.20	$0.104^{+0.240}_{-0.090}$
8	7.90 ± 0.25[b]	$41.9^{+20.6}_{-14.5}$[b]
	8.40 ± 0.25	$8.91^{+2.49}_{-2.08}$
	8.90 ± 0.25	$3.56^{+1.19}_{-0.95}$
	9.35 ± 0.20	$1.11^{+0.57}_{-0.42}$
	9.75 ± 0.20	$0.591^{+0.371}_{-0.262}$
	10.15 ± 0.20	$0.0711^{+0.1637}_{-0.0617}$
9[c]	7.50 ± 0.50[b]	$29.1^{+23.0}_{-13.9}$[b]
	8.25 ± 0.25	$3.67^{+2.93}_{-1.81}$
	8.75 ± 0.25	$0.738^{+0.348}_{-0.256}$
	9.50 ± 0.50	$0.0764^{+0.1016}_{-0.0517}$
10	7.65 ± 0.35[b]	$12.0^{+15.8}_{-7.8}$[b]
	8.25 ± 0.25	$0.264^{+0.258}_{-0.146}$
	8.75 ± 0.25	$0.0872^{+0.1997}_{-0.0729}$

Notes.
[a] Central value and range of each stellar mass bin.
[b] This mass bin is dominated by sources with S/N < 2 in either IRAC bands and lies below our fiducial completeness threshold (Section 5), making the corresponding volume density very uncertain (open points in Figure 7).
[c] Stellar mass estimates at $z \sim 9$ are particularly challenging to constrain with current observations because the uncertainties in photometric redshifts do not allow us to ascertain where the 3.6 μm band lies relative to the Balmer Break, i.e., whether contributions to the 3.6 μm band are primarily the rest-frame UV or the rest-frame optical or a combination of the two. A separate but similar challenge for $z \sim 9$ galaxies is the lack of knowledge as to the degree to which the 4.5 μm band is contaminated by strong nebular line emission.

much clearer thanks to its being mostly orthogonal to the degeneracy between the two parameters. A similar result was found by, e.g., Grazian et al. (2015) for $z \sim 4$–7. This suggests that the evolution of the SMF between $z \sim 8$ and $z \sim 6$ proceeded both in stellar mass and in number density.

Our measurements suggest a constant slope $\alpha \sim -1.8$ between $z \sim 6$ and $z \sim 8$, and are generally consistent at $\lesssim 2\sigma$ with previous results (Figure 9; e.g., Duncan et al. 2014; Song et al. 2016; Bhatawdekar et al. 2019; Kikuchihara et al. 2020). Our characteristic stellar masses are lower by ~ 0.2–0.5 dex
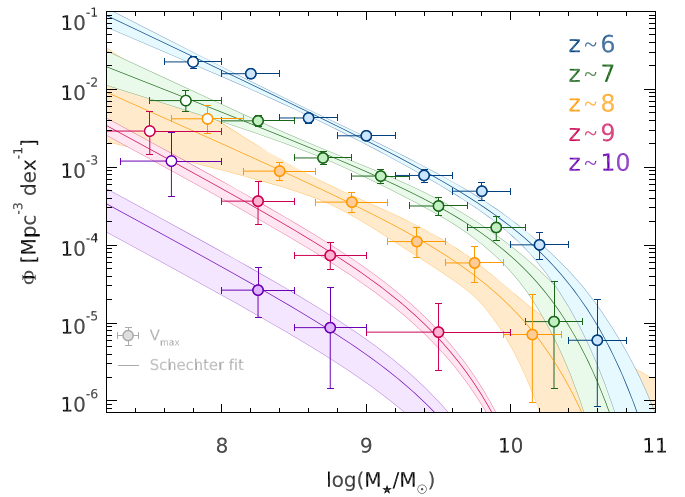

Figure 7. The colored circles with error bars correspond to our $V_{\rm max}$ estimates of the SMF from $z \sim 6$ to $\sim$10, following the color scheme presented in the legend at the top right corner of the figure. The open circles at the lowest masses identify those measurements corresponding to stellar masses below our confidence threshold (Section 5). These low-mass points have large, uncertain corrections. The solid colored curves mark the best-fitting Schechter functions, while the filled areas show those regions preferred at 68% confidence.

Table 5
SMF Schechter Fit Parameters

Redshift Bin	α	$\log(\mathcal{M}_\star^*/\mathcal{M}_\odot)$	$\log(\phi^*/{\rm dex}^{-1}/{\rm Mpc}^{-3})$
6	$-1.88^{+0.06}_{-0.03}$	$10.24^{+0.08}_{-0.11}$	$-4.09^{+0.17}_{-0.12}$
7	$-1.73^{+0.08}_{-0.08}$	$10.04^{+0.15}_{-0.13}$	$-4.14^{+0.19}_{-0.23}$
8	$-1.82^{+0.20}_{-0.21}$	$9.98^{+0.44}_{-0.24}$	$-4.69^{+0.40}_{-0.72}$
9	-2.00 [fixed]	9.50 [fixed]	$-5.12^{+0.10}_{-0.13}$
10	-2.00 [fixed]	9.50 [fixed]	$-6.13^{+0.19}_{-0.36}$

Note. Letting $\mathcal{M}_\star^*$ vary in the $z \sim 9$ fit gives a very similar $\mathcal{M}_\star^* = 10^{9.54} M_\odot$.

compared to previous results at $z \sim 6$–8. This may be due to the lower number density of the most massive galaxies that we find compared to the literature. While our estimates are supported by the unique deep wide-area coverage in the rest-frame optical, robustly constraining the massive end of the SMF would require combining data sets with depth and area similar to those considered in this study with others covering $\gtrsim 10 \times$ larger areas than those currently available, making the above consideration only an informed speculation. Encouragingly, the recent Spitzer Matching Survey of the Ultra-VISTA Deep Stripes (SMUVS; Caputi et al. 2017; Ashby et al. 2018), COMPLETE (PI: Labbé), and COMPLETE2 (PI: Stefanon) programs are providing coverage with deep ($\gtrsim 40$ hr, corresponding to 1σ nominal sensitivity of $\sim$30 nJy) Spitzer/IRAC data over a large patch of the sky ($\sim$0.8 degree[2] when all observations from the three programs are combined) across the COSMOS/UltraVISTA footprint. These programs will allow for the future characterization of the massive end of the SMF at $z \geqslant 6$. Finally, our estimate of the number density normalization parameter suggests a smooth decrease with increasing redshift, similar to what is seen by others.

The Schechter parameterizations are useful for a synthetic representation of the SMFs. In Section 6.3, we compare our $V_{\rm max}$ measurements to the corresponding ones from the literature.
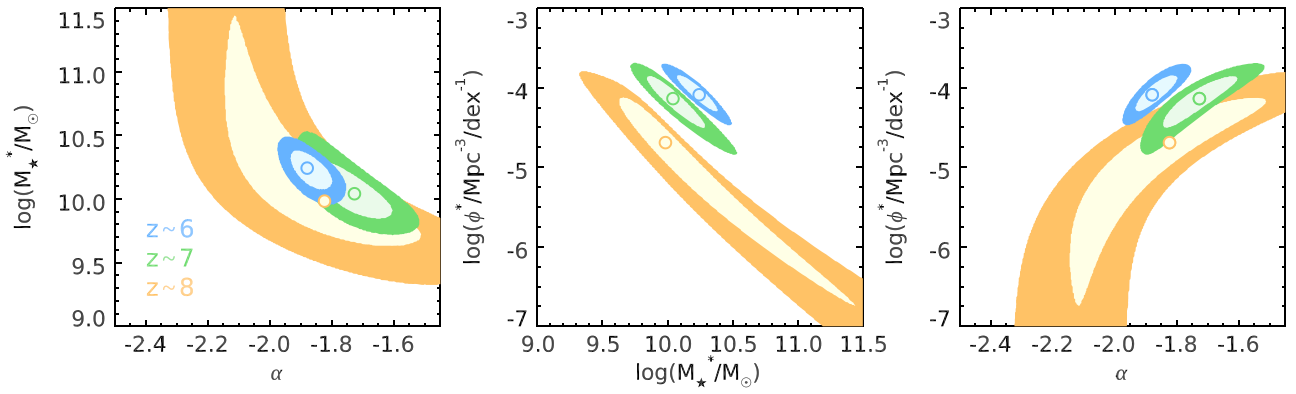
Figure 8. 68% and 95% confidence intervals (light- and dark-shaded contours, respectively) for the best-fit Schechter parameters describing our SMFs at $z \sim 6$, $z \sim 7$ and $z \sim 8$ (blue, green and orange contours, respectively). The colored circles mark the best-fit values at each redshift. The large uncertainties associated with the Schechter parameters prevent any unambiguous assessment of the evolution of the SMF from $z \sim 8$ to $z \sim 6$; however, there is clear evidence for a positive evolution in the characteristic stellar mass $\mathcal{M}_\star^*$ and normalization factor ϕ^* with cosmic time.

6.2. Other Uncertainties Potentially Affecting the SMF Measurements

6.2.1. Gravitational Lensing

One potential source of uncertainty for high-redshift galaxy SMF determinations arises due to the impact of gravitational lensing from foreground galaxies. Lensing magnification can systematically increase both the apparent brightness and stellar mass estimates of individual distant galaxies. While this effect is most evident when the lens is a cluster of galaxies (e.g., the Hubble Frontier Field program; Lotz et al. 2017), one could still expect gravitational lensing to significantly impact the LFs and SMFs estimates of field galaxies at $z > 4$, given the much larger surface density of galaxies at $z < 4$ compared to $z > 4$ (e.g., Bouwens et al. 2021).

This issue has already been considered in substantial previous work (e.g., Pei 1993; Lima et al. 2010; Wyithe et al. 2011; Fialkov & Loeb 2015; Mason et al. 2015a). In particular, Fialkov & Loeb (2015) quantified the impact of gravitational lensing on the estimates of $6 < z < 15$ LFs using a semi-analytical framework. Their results indicate a strong systematic impact at the high luminosity end of the UV LF ($M_{UV} \lesssim -24.5$ mag) but negligible contributions ($\lesssim 1\%$) for sources fainter than $M_{UV} \sim -21.5$ mag (see also Mason et al. 2015b, who arrived at qualitatively similar results using the $z \sim 8$ UV LF). Guided by these findings and considering that our samples only include sources with UV luminosities M_{UV} of ~ -22 mag and fainter, no correction is made to our SMF results for gravitational lensing. Such a treatment is consistent with what we find in Stefanon et al. (2019) and Oesch et al. (2014) for the brightest $z \sim 8$ and $z \sim 10$ galaxies in looking for possible lensing magnification by foreground sources. In Oesch et al. (2014), for example, the apparent lensing magnification only appeared to be marginal for two sources (corresponding to excesses of ~ 0.02 dex and 0.04 dex in stellar mass, for GN-z10-1 and GN-z10-2, respectively).

6.2.2. Photometric Redshifts

The stellar masses discussed in Section 3 were computed assuming that the redshift of each source was equal to its photometric redshift. In reality, however, there exists a range of possible redshifts for each source given by the redshift likelihood distribution $P(z)$, which would allow for a range of plausible stellar masses. This scatter could add to the uncertainties in our SMF measurements.
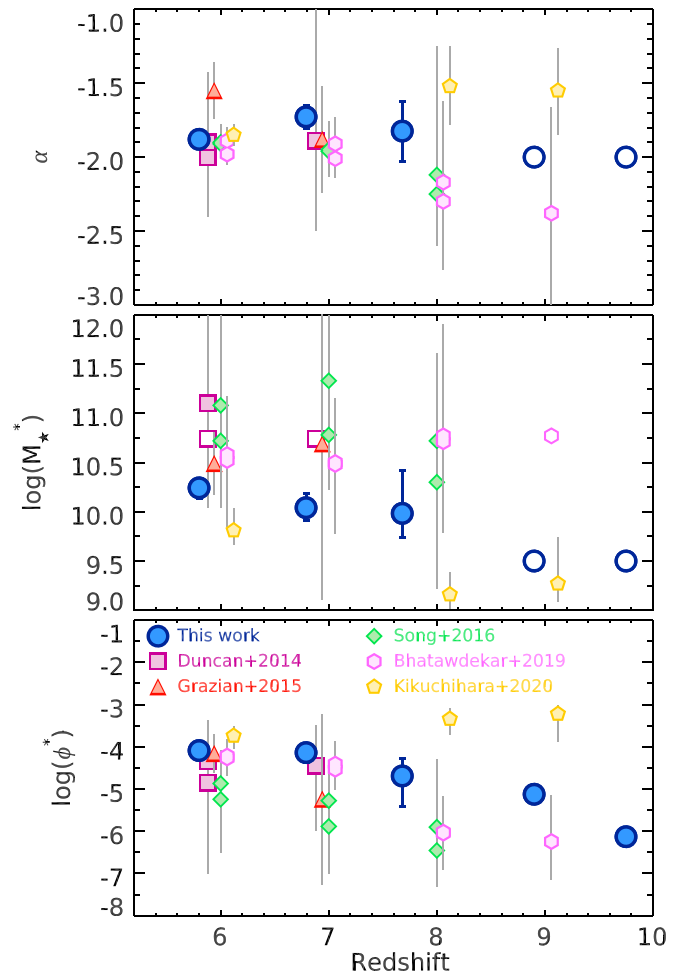

Figure 9. Evolution derived for ϕ^*, $\mathcal{M}_\star^*$, and α from $z \sim 10$ to $z \sim 6$ and a comparison to other determinations of these parameters from Duncan et al. (2014, magenta squares), Grazian et al. (2015, red triangles), Song et al. (2016, green diamonds), Bhatawdekar et al. (2019, pink hexagons), and Kikuchihara et al. (2020, yellow pentagons) over the redshift range $z \sim 6$–10. Open symbols show cases where some parameter values were kept fixed during the fit (see text).

We estimated the impact of individual $P(z)$ on our derived SMF using Monte Carlo simulations. For each source, we computed a new stellar mass at the redshift randomly drawn
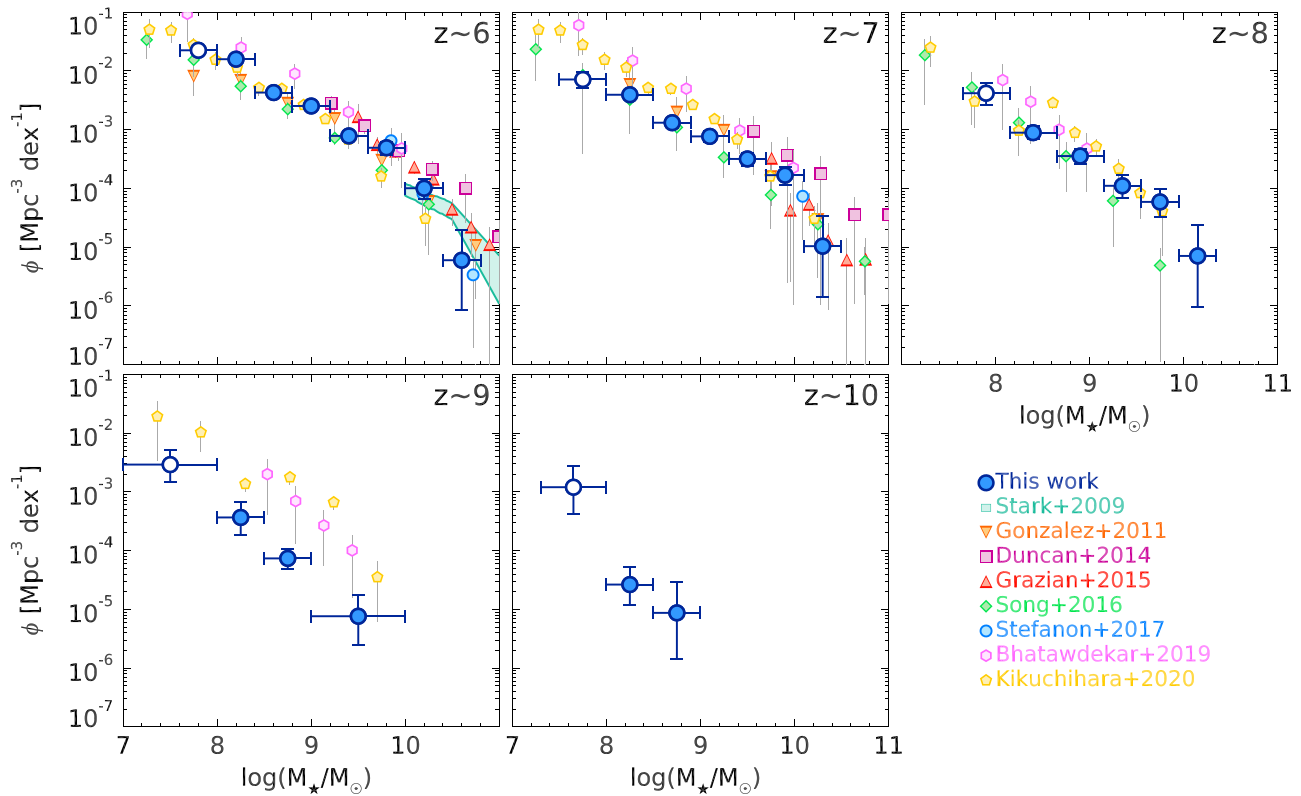
Figure 10. Comparison of the SMF estimates from this work to previous determinations. Specifically, we here consider the SMFs of Stark et al. (2009), González et al. (2011), Grazian et al. (2015), Duncan & Conselice (2015), Song et al. (2016), Stefanon et al. (2017), Bhatawdekar et al. (2019) and Kikuchihara et al. (2020), as listed in the legend in the lower right. We converted those stellar masses based on the Chabrier (2003) IMF into a Salpeter (1955) IMF through a 1.7 multiplicative factor. The redshift for each SMF panel is indicated in the top right corner.

from the corresponding $P(z)$, replicating the procedures described in Section 3, depending on the specific redshift and significance of the flux density estimate in the IRAC bands. New SMFs were then constructed using the new stellar masses as input. We repeated this procedure 100 times and evaluated the 16th and 84th percentiles on the volume densities. This process resulted in median uncertainties of ~0.06, 0.08, 0.1, 0.2, and 0.2 dex for the SMFs at $z \sim 6$, 7, 8, 9, and 10, respectively. These uncertainties indicate that the overall error budget of the SMFs are dominated by the combination of Poisson and cosmic variance effects, with a negligible contribution from the redshift probability distribution of the individual sources. We therefore concluded the uncertainties we derive on the SMFs are accurate and are not substantial underestimates.

6.3. Comparison to Previous Estimates

In Figure 10, we compare our V_{max} estimates to previous studies. The large number of sources in our SMFs from the larger HST data set, combined with the much deeper IRAC GREATS data set, enabled us to generate SMFs at $z \sim 6-10$ that have robust rest-frame optical underpinnings and improved sample statistics. Specifically, we show the results of Stark et al. (2009), González et al. (2011), Duncan et al. (2014), Grazian et al. (2015), Song et al. (2016), Stefanon et al. (2017), Bhatawdekar et al. (2019), and Kikuchihara et al. (2020). We applied a factor of 1.7 (Madau & Dickinson 2014) to convert those stellar masses originally computed with a Chabrier (2003) IMF into a Salpeter (1955) IMF.

At $z \sim 6$, for $\mathcal{M}_\star > 5 \times 10^9 M_\odot$ our SMF is consistent at ~1σ with the estimates of Stark et al. (2009), González et al. (2011), Grazian et al. (2015), Stefanon et al. (2017), Bhatawdekar et al. (2019), and Kikuchihara et al. (2020), while there is a somewhat larger $\gtrsim 2\sigma$ tension with the measurements of Duncan et al. (2014). Our low-mass end is consistent with the SMF of González et al. (2011), Song et al. (2016), and Kikuchihara et al. (2020), with marginal indication of lower volume densities than Bhatawdekar et al. (2019) and more consistent with Duncan et al. (2014). At $z \sim 7$ and $z \sim 8$, there is an increased scatter among the measurements in the literature and larger uncertainties. Our $z \sim 7$ SMF estimate lies among the current measurements for $\mathcal{M}_\star \gtrsim 10^9 M_\odot$, while for lower stellar masses, our SMF lies closer to the measurements of González et al. (2011) and Song et al. (2016). At $z \sim 8$, our measurements at $\mathcal{M}_\star \lesssim 10^9 M_\odot$ also fall among the estimates of Song et al. (2016), Bhatawdekar et al. (2019), and Kikuchihara et al. (2020), while at higher stellar masses the measurements of Kikuchihara et al. (2020) are more consistent with our results.

At $z \sim 9$, our $\mathcal{M}_\star \sim 10^9 M_\odot$ measurement is lower by ~1 dex than other recent estimates of Bhatawdekar et al. (2019) and Kikuchihara et al. (2020), while our measurement at higher mass is consistent with that of Kikuchihara et al. (2020). We remind the reader that estimating stellar masses at $z \sim 9$ is very difficult because the large uncertainties in photometric redshifts do not properly allow us to ascertain where the 3.6 μm band falls relative to the Balmer break, and so we cannot define the relative contributions above ("optical") and below ("UV") the break. At $z \sim 9$ in the 4.5 μm band there is the additional

Table 6
Stellar and Dark Matter Halo Mass Densities

Nominal redshift	Median redshift	$\log(\rho_\star/\mathcal{M}_\odot/\mathrm{Mpc}^{-3})$[a]	$\log(\rho_h/\mathcal{M}_\odot/\mathrm{Mpc}^{-3})$[b]	$\log(\mathcal{M}_{h,lim}/\mathcal{M}_\odot)$[c]	$\log(\rho_h/\rho_\star)$[d]
6	5.80	$6.68^{+0.09}_{-0.11}$	$8.64^{+0.10}_{-0.03}$	$10.46^{+0.05}_{-0.11}$	$1.95^{+0.15}_{-0.10}$
7	6.79	$6.26^{+0.13}_{-0.17}$	$8.20^{+0.09}_{-0.05}$	$10.54^{+0.05}_{-0.09}$	$1.93^{+0.19}_{-0.14}$
8	7.68	$5.73^{+0.21}_{-0.33}$	$7.69^{+0.11}_{-0.06}$	$10.55^{+0.08}_{-0.10}$	$1.96^{+0.35}_{-0.22}$
9	8.90	$4.89^{+0.25}_{-0.29}$	$6.97^{+0.20}_{-0.16}$	$10.47^{+0.09}_{-0.12}$	$2.08^{+0.36}_{-0.30}$
10	9.75	$3.68^{+0.52}_{-0.79}$	$6.04^{+0.20}_{-0.22}$	$10.72^{+0.08}_{-0.10}$	$2.35^{+0.81}_{-0.56}$

Notes.
[a] Logarithm of the stellar mass density, obtained integrating the SMF down to a stellar mass limit of $\mathcal{M}_\star = 10^8 \mathcal{M}_\odot$.
[b] Logarithm of the dark matter halo mass density, obtained by integrating the HMF down to a halo mass limit of $\mathcal{M}_h = \mathcal{M}_{h,lim}$ (see note c below).
[c] Logarithm of the halo mass obtained from our abundance matching procedure, used as a lower limit in the measurement of the halo mass density.
[d] Ratio between the measured halo and the stellar mass densities, in log units.

challenge of unknown levels of contamination by the strong nebular lines ([O II] or [O III]+Hβ). The discrepancies observed at $z \sim 9$ should therefore be viewed with more caution. We are not aware of any other SMF estimates based on samples at $z \sim 10$.

7. Discussion

7.1. Dispersion of SMF Measurements

The compilation of estimates presented in Figure 10 shows an overall good agreement. However, for some redshifts and/or mass bins systematic differences can be as large as ~ 0.5–1.0 dex. A thorough analysis of the causes of these systematic differences goes beyond the scope of this paper. Here, we limit our comments to briefly outline some possible causes.

A first potential effect could be systematics in stellar mass estimates from different studies as a result of the different assumptions on the star formation history (e.g., constant versus exponential or delayed SFH; e.g., Michałowski et al. 2014; Mobasher et al. 2015; Leja et al. 2019; Lower et al. 2020) and nebular emission (e.g., Stark et al. 2013). Furthermore, as already discussed by Duncan et al. (2014), photometric redshift selected samples (e.g., Duncan et al. 2014; Grazian et al. 2015; Song et al. 2016; Bhatawdekar et al. 2019) potentially include redder sources, which are usually excluded by the LBG criteria (e.g., Stark et al. 2009; González et al. 2011; Stefanon et al. 2017; Kikuchihara et al. 2020), resulting in higher volume densities for the SMFs of photometric redshift-selected samples. However, this is not always the case here: for instance, the photometric redshift-selected SMF at $z \sim 6$ of Song et al. (2016) is consistently lower than the LBG-based SMF of Kikuchihara et al. (2020). One further possibility was discussed by Vulcani et al. (2017) and results from the contamination of LBG samples by lower-redshift interlopers. This particularly affects faint sources lacking sufficiently deep imaging at wavelengths bluer than the nominal Lyman break. Finally, cosmic variance may have significant impact at the highest redshifts (e.g., Bhowmick et al. 2020) because the photometric depth necessary to constrain the samples is only available over small ($\lesssim 100\,\mathrm{arcmin}^2$) areas.

7.2. Stellar Mass Density

We computed our SMD from $z \sim 6$ to $z \sim 10$ from the best-fit Schechter functions down to a consistent lower mass limit of

$\mathcal{M}_\star = 10^8 \mathcal{M}_\odot$. The full set of measurements can be found in Table 6 and are presented in Figure 11.

In the same figure we also show recent estimates from the literature. Specifically, we include the compilation of Madau & Dickinson (2014) with the estimates of Li & White (2009), Gallazzi et al. (2008), Moustakas et al. (2013), Bielby et al. (2012), Pérez-González et al. (2008), Ilbert et al. (2013), Muzzin et al. (2013), Arnouts et al. (2007), Pozzetti et al. (2010), Kajisawa et al. (2009), Marchesini et al. (2009), Reddy et al. (2012), Caputi et al. (2011), González et al. (2011), Lee et al. (2012), Yabe et al. (2009), and Labbé et al. (2013), and measurements from Oesch et al. (2014), Duncan et al. (2014), Grazian et al. (2015), Song et al. (2016), Davidzon et al. (2017), Bhatawdekar et al. (2019), and Kikuchihara et al. (2020).

At $z \sim 6$ and $z \sim 7$, there is good consistency between the measurements from Grazian et al. (2015), Song et al. (2016), and Kikuchihara et al. (2020) and our results, but those of Duncan et al. (2014) and Bhatawdekar et al. (2019) are somewhat higher, even though the large error bars at $z \sim 7$ make all the results formally consistent. Our results are also consistent with the pioneering determinations of the SMD at $z \sim 6 - 7$ of Yan et al. (2006), Labbé et al. (2006), and Eyles et al. (2007). At $z \sim 8$, the large uncertainties make essentially all the existing measurements consistent with ours, as well as those of Labbé et al. (2013), Song et al. (2016), Bhatawdekar et al. (2019), and Kikuchihara et al. (2020), despite systematic differences of $\gtrsim 0.5$ dex. At $z \sim 9$, the current estimates of Bhatawdekar et al. (2019) and Kikuchihara et al. (2020) lie above ours. This is not surprising, considering that our $z \sim 9$ SMF is lower by ~ 1 dex than the corresponding SMF from those studies. Finally, at $z \sim 10$, our measurement is ~ 0.35 dex lower than the previous measurement of Oesch et al. (2014), but the two are consistent at 1σ.

Our results between $z \sim 10$ and $z \sim 6$ suggest a smooth evolution of the SMD, with an indication of more rapid evolution occurring in the first ~ 500–$600\,\mathrm{Myr}$ of cosmic time up to $z \sim 8$. Our SMD from $z \lesssim 8$ to $z \sim 6$ is consistent with an exponential increase with the redshift, with a slope of $(-0.52 \pm 0.11)z$, steeper than the $\sim -0.28z$ observed at $z \sim 0$–3 by McLeod et al. (2021) and marginally consistent (1.5σ) with the $-0.36z$ dependence found by Dayal & Ferrara (2018) for $4 < z < 10$. At $z \sim 10$, our SMD value lies below the extrapolation of the relation that is seen from $z \lesssim 8$ to later times, indicating a fast buildup of stellar masses at these very early epochs. Strikingly, only a tiny fraction ($\sim 5 \times 10^{-6}$) of today's stellar mass was already in place at $z \sim 10$. By $z \sim 6$
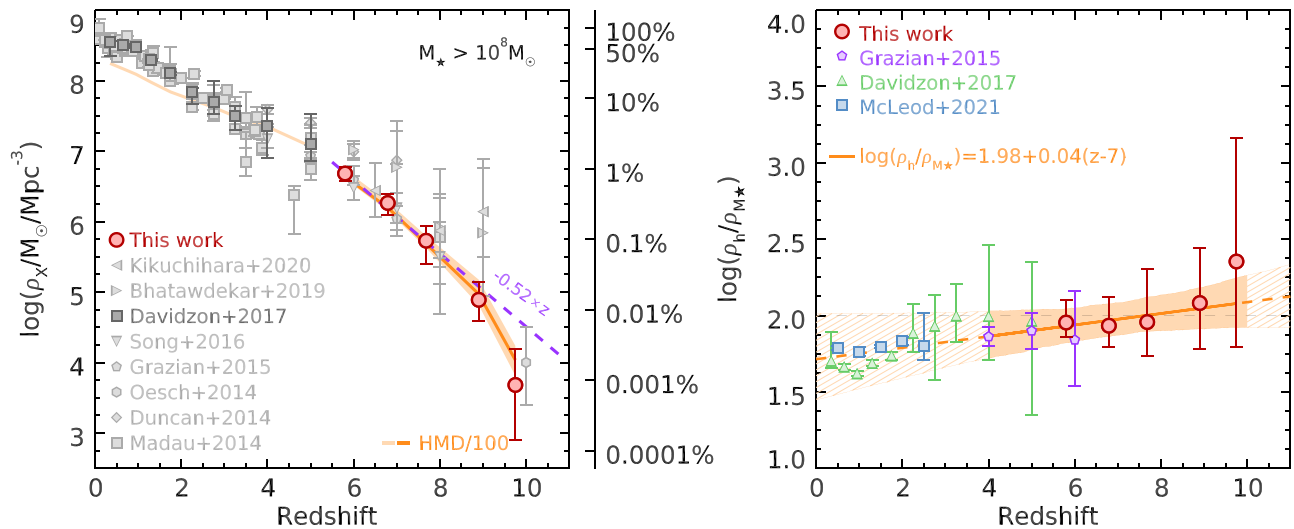
Figure 11. (Left): Evolution of the stellar mass density (for galaxies with $\mathcal{M}_\star \geqslant 10^8 \mathcal{M}_\odot$) over $\sim$13.5 Gyr. The red filled circles correspond to our SMD values, with the purple dashed line being the fit to our values for redshifts less than $z \sim 8$. The gray symbols mark existing measurements as indicated by the legend, converted to the Salpeter (1955) IMF, where necessary, and include the compilation of Madau & Dickinson (2014)—see text for details—and measurements from Oesch et al. (2014), Duncan et al. (2014), Grazian et al. (2015), Song et al. (2016), Davidzon et al. (2017), Bhatawdekar et al. (2019), and Kikuchihara et al. (2020). The orange curves correspond to the mass density of dark matter halos, rescaled by a factor $1/100$, recovered from abundance matching the SMF from this work at $z \sim 6$, 7, 8, 9, and 10 (dark orange curve) and the SMF of Davidzon et al. (2017) at $z < 5$ (light orange curve). The additional vertical axis on the right indicates the fraction of the stellar mass density relative to that in the local universe. (Right): Ratio between the halo mass density and the stellar mass density, computed from our SMF measurements (filled red circles) and from the SMFs of Grazian et al. (2015), Davidzon et al. (2017), and McLeod et al. (2021), as indicated by the legend. All HMD and SMD measurements were performed applying the same method (see Sections 7.2 and 7.3.1). We excluded from our analysis the HMD at $z \sim 3.25$ of McLeod et al. (2021) and at $z \sim 7$ of Grazian et al. (2015) given that those estimates are essentially undetermined in our analysis. The orange line and shaded region correspond to the linear fit to the $z \geqslant 4$ measurements and 68% confidence interval, respectively. These results suggest only a marginal evolution of the ratio $\rho_\mathrm{h}/\rho_\star \sim 100$ from $z \sim 10$ to $z \sim 3$–4, and with minimal change even to $z \sim 0$.

(i.e., when the universe was only $\sim$1 Gyr old, or just $\sim$500 Myr after the epoch corresponding to $z \sim 10$), the density had increased by $\sim$1000$\times$ from $z \sim 10$! The resulting SMD was then $\sim$1%–2% of today's value. The evolution that followed happened at a much slower pace after $z \sim 6$, requiring $\sim$13 Gyr ($\sim$93% of cosmic history) for the SMD to grow the final factor $\sim$50–100.

7.3. Dark Matter Halos

According to the concordance galaxy formation scenario (e.g., Rees & Ostriker 1977; White & Rees 1978; Fall & Efstathiou 1980—see also Baugh 2006 for a review), the assembly of stellar mass at early times is driven by the accretion of dark matter halos, which, in turn, drive the accretion of cold gas onto the galaxy. The gas is finally converted into stars, modulo an efficiency, which in general can depend on the mass of the dark matter halo. In this section, we leverage our SMF estimates to probe the relation between stellar mass and halo mass in the first $\sim$1 Gyr of cosmic history.

7.3.1. Halo Mass Density

We applied abundance matching techniques (Kravtsov et al. 2004; Tasitsiomi et al. 2004; Vale & Ostriker 2004; Conroy et al. 2006) to our SMF estimates to evaluate whether the rapid growth of the SMD observed in Figure 11 is matched by that of the dark matter halos.

Dark matter halos can undergo more significant stripping before being accreted than their baryonic counterparts (Conroy et al. 2006; Trujillo-Gomez et al. 2011; Reddick et al. 2013; Campbell et al. 2018; Wechsler & Tinker 2018). Given this, recent work suggests that the peak maximum velocity of the

particles in the dark matter halo across its formation history (commonly denoted as V_{peak}), or the maximum circular velocity of a halo at the time of accretion (v_{acc}), constitute a better match to the baryonic properties of galaxies and can better reproduce the two-point correlation function (e.g., Conroy et al. 2006; Reddick et al. 2013). For our exercise, we therefore matched the cumulative densities of the SMF to $\mathcal{M}_\star = 10^8 \mathcal{M}_\odot$ to those of v_{acc} provided by the Bolshoi N-body numerical simulation (Klypin et al. 2016). In particular, we adopted the Bolshoi–Planck run, based on the Planck Collaboration et al. (2014) ΛCDM cosmology with parameters $h = 0.677$, $\Omega_m = 0.307$, $\Omega_\Lambda = 0.693$, $n_s = 0.96$, and $\sigma_8 = 0.823$.[11] The simulation was run in a box of side of $250 h^{-1}$ Mpc and includes 2048^3 particles, allowing us to resolve halos with a mass of $10^{10} \mathcal{M}_\odot$ (see Klypin et al. 2016; Rodríguez-Puebla et al. 2016 for details on the simulation). Dark matter halo masses and 68% confidence intervals were then obtained as the median and 16th- and 84th-percentiles of the halo masses were included in the range of the recovered v_{acc}. The results of this procedure are reported in Table 6. We also repeated the abundance matching procedure adopting the halo mass functions of Behroozi et al. (2013) generated by the HMFcalc

---

[11] The cosmological parameters adopted for the Bolshoi simulation differ from our 0.7, 0.3, 0.7 fiducial cosmology. These differences systematically affect the estimates of volume densities and stellar masses and could therefore potentially affect our abundance matching analysis. Adopting $h = 0.67$ instead of $h = 0.7$ would result in stellar masses larger by $\sim$0.03 dex. The corresponding shift of the SMFs would mimic an increase of the volume densities ($\sim$+0.054 dex for $\alpha = -1.8$). However, for $h = 0.67$, the volume densities would be smaller by $\sim$0.04 dex, mitigating most of the apparent increase in volume density resulting from the higher stellar masses. The differences in Ω_Λ and Ω_m result in even smaller corrections. Such very small residual differences allow us to conclude that our abundance matching results are robust against the marginal differences between the cosmological parameters used for our SMF estimates and those adopted for the Bolshoi simulation.

tool (Murray et al. 2013) and found that the halo masses differ by $\lesssim 0.04$ dex from those computed with the v_{acc} abundance, increasing our confidence in the results.

While the halo mass densities are ~ 2 orders of magnitude higher than the corresponding stellar mass densities, it is quite informative to compare the *rate* at which they grow to that of the SMD. Therefore, in Figure 11 (Left), we plot the halo mass densities after rescaling them by a factor 0.01. It is striking that, despite the large uncertainties, particularly at the highest redshifts, the growth of the SMD follows that of the halo mass; in particular, between $z \sim 6$ and $z \sim 9$, there seems to be an almost 1:1 relation between the two rates. We repeated the same procedure at lower redshifts adopting the SMF of Davidzon et al. (2017). The resulting halo mass density (HMD) estimates, after being rescaled by the same 0.01 factor, are marked in Figure 11 (left) with the lighter orange curve. Because of the limited depth available for the SMFs of Davidzon et al. (2017), we compare, in the right panel of Figure 11, our measurements of the ratio of the SMD and the dark matter halo density to those we obtain with the same procedure using the SMFs of Grazian et al. (2015), Davidzon et al. (2017), and McLeod et al. (2021). These measurements show that the rate of growth of the stellar mass assembly is still very similar to that of the dark matter halos down to $z \sim 4$. The marginal evolution is confirmed by a linear fit to the logarithm of the ratio between the two densities at $z \geqslant 4$, resulting in:

$$\log(\rho_{\mathrm{h}}/\rho_{\mathcal{M}_\star}) = (1.976 \pm 0.104) + (0.037 \pm 0.041) \times (z - 7).$$
(6)

Remarkably, our analysis shows that the stellar and halo mass densities show a consistent trend in their ratio to $z \sim 0$, with both having increased by five orders of magnitude between $z \sim 10$ and $z \sim 0$. Nonetheless, their ratio in Figure 11 (right) has changed by a strikingly small 0.3–0.5 dex over this same redshift range ($\sim 96\%$ of cosmic history), especially when compared to the ~ 5 dex growth in both ρ_{h} and $\rho_\star$.

The above results are qualitatively consistent with the coevolution between the star formation rate density and the halo mass accretion rate recently found by Oesch et al. (2018), indicating a scenario where the efficiency of star formation remained approximately constant through the first ~ 1.5 Gyr of cosmic history, as also suggested by some of the recent models (e.g., Mason et al. 2015a; Mashian et al. 2016; Wilkins et al. 2017; Bhowmick et al. 2018; Ma et al. 2018; Tacchella et al. 2018; Park et al. 2019; Bouwens et al. 2021; Hutter et al. 2021) and observations (e.g., Durkalec et al. 2015; Stefanon et al. 2017; Harikane et al. 2018). These results are also qualitatively consistent with the coevolution between the specific SFR and the specific dark matter halo mass accretion rate found in recent studies (e.g., Stefanon et al. 2021a).

7.3.2. Stellar-to-halo Mass Ratio

The ratio between the stellar and the halo mass is a proxy for the efficiency of the conversion of cold gas into stars (but see, e.g., Romeo et al. 2020 and references therein for a different perspective on the study of the connection between stellar and halo masses). The coevolution between dark matter halos and stellar mass presented in the previous section is dominated by galaxies with $\mathcal{M}_\star \sim 10^8 \mathcal{M}_\odot$ because of their larger volume densities. In this section, we explore in more detail the relation between the stellar mass and halo mass across the range of stellar masses probed in our SMF estimates.

We adopted the abundance matching tools discussed in the previous section to estimate the dark matter halo masses for each specific stellar mass bin. However, for this analysis we are not constrained to match the same limit in stellar mass across the different redshifts, as instead it was the case for the SMD discussed in Section 7.2. We therefore computed the reference cumulative densities by numerically integrating our V_{max} measurements in correspondence of each value in stellar mass. For this, we adopted the center of the stellar mass bin as reference value, reducing by 50% the amplitude of the lowest stellar mass bin in each computation. Our results do not significantly differ when we use the Schechter parameterizations instead of the v_{max} estimates. We set the uncertainties in stellar mass to 68% ($\pm 34\%$) of the width of the corresponding stellar mass bin, assuming an approximately uniform distribution of stellar mass within each stellar mass bin. The resulting halo masses and SHMR are listed in Table 7 and are graphically presented in Figure 12.

Our measurements indicate a monotonic increase at all redshifts, as expected from the extrapolation of results at lower redshifts (see, e.g., Wechsler & Tinker 2018; Legrand et al. 2019; Girelli et al. 2020 and references therein). Remarkably, the ($\mathcal{M}_\star$, $\mathcal{M}_{\mathrm{halo}}$) pairs computed for each redshift $z \sim 6$, 7, 8, 9, and 10 overlap within the nominal uncertainties over most of the range in halo masses. This further supports our result of an essentially constant efficiency of star formation at these epochs. Nonetheless, the $z \sim 9$ and $z \sim 10$ estimates have a lower significance (~ 1–2σ), potentially hiding any evolution in the first ~ 600 Myr.

Because our ($\mathcal{M}_\star$, $\mathcal{M}_{\mathrm{halo}}$) measurements do not strongly depend on redshift, we fitted the following parametric form (Moster et al. 2010; see also Yang et al. 2003) after merging all sets of measurements:

$$\frac{\mathcal{M}_\star}{\mathcal{M}_{\mathrm{halo}}} = 2N \left[\left(\frac{\mathcal{M}_{\mathrm{halo}}}{\mathcal{M}_c} \right)^{-\beta} + \left(\frac{\mathcal{M}_{\mathrm{halo}}}{\mathcal{M}_c} \right)^{\gamma} \right]^{-1}.$$
(7)

Here, N is a normalization factor, $\mathcal{M}_c$ is the characteristic halo mass where the star formation efficiency is maximized, while β and γ are the slopes of the low-mass and high-mass regimes, respectively. Given that our range in mass does not probe masses larger than $\approx \mathcal{M}_c$ needed to constrain γ, we assumed $\gamma = 0.4$ (Tacchella et al. 2018). For this same reason, our constraints on $\mathcal{M}_c$ should be taken with caution. Our fit results in $\beta = 1.35 \pm 0.26$, $\log \mathcal{M}_c / \mathcal{M}_\odot = 11.5 \pm 0.2$ and $N = 0.0297 \pm 0.0065$. The corresponding parameterization is presented in Figure 12 with the solid gray curve.

In Figure 13, we compare our estimates with existing determinations. Specifically, at $z \sim 6$ and $z \sim 7$ we included the measurements of Finkelstein et al. (2015b), which are based on abundance matching the UV LF, the estimates of Harikane et al. (2018), which rely on the two-point correlation function of LBGs, and those of Stefanon et al. (2017) obtained applying the abundance matching to the rest-frame optical LF. The estimates of Finkelstein et al. (2015b) and Tacchella et al. (2018) assumed a WMAP7 cosmology (Komatsu et al. 2011), shifting the halo masses toward higher values. Given this, we converted them to the Planck Collaboration et al. (2016) cosmology applying the correction described in Appendix D. Furthermore, we multiply by a factor 1.7 the stellar-to-halo mass values of Harikane et al. (2018) to convert them from a Chabrier (2003) to a Salpeter (1955) IMF. To our knowledge,
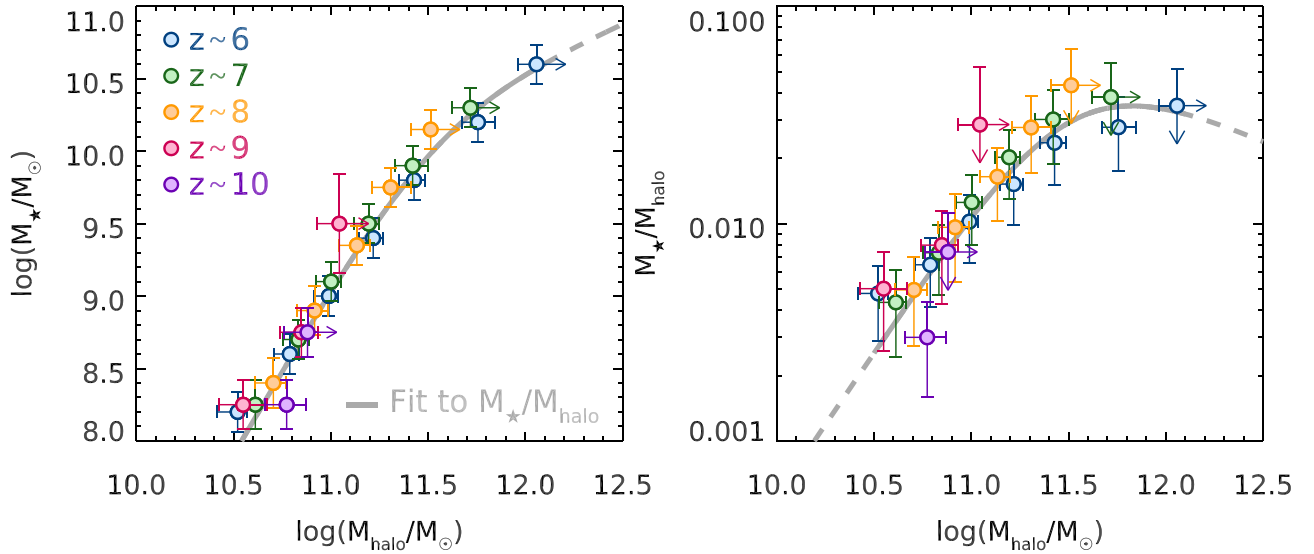
Figure 12. (Left:) Stellar mass as a function of the halo mass recovered from abundance matching the V_{max} estimates of the SMF presented in this work. Each color refers to a specific redshift bin as labeled at the top left corner. (Right panel:) Ratio between the stellar mass and the halo mass, as a function of the halo mass, for the same redshift bins presented in the left-side panel. Our results are consistent with marginal evolution, or even no evolution at all, of the stellar-to-halo mass ratio between $z \sim 10$ and $z \sim 6$. The gray curve corresponds to our best-fit $\mathcal{M}_\star/\mathcal{M}_{halo}$ parameterization (see Equation (7)), fitted to all the redshift-merged estimates. The solid points with arrows mark those halo mass measurements whose lower uncertainty could not be determined because of the limited range available for v_{acc}. The overlap of $\mathcal{M}_\star/\mathcal{M}_{halo}$ across the redshift range of our study indicates that the star formation efficiency does not evolve in the first Gyr.
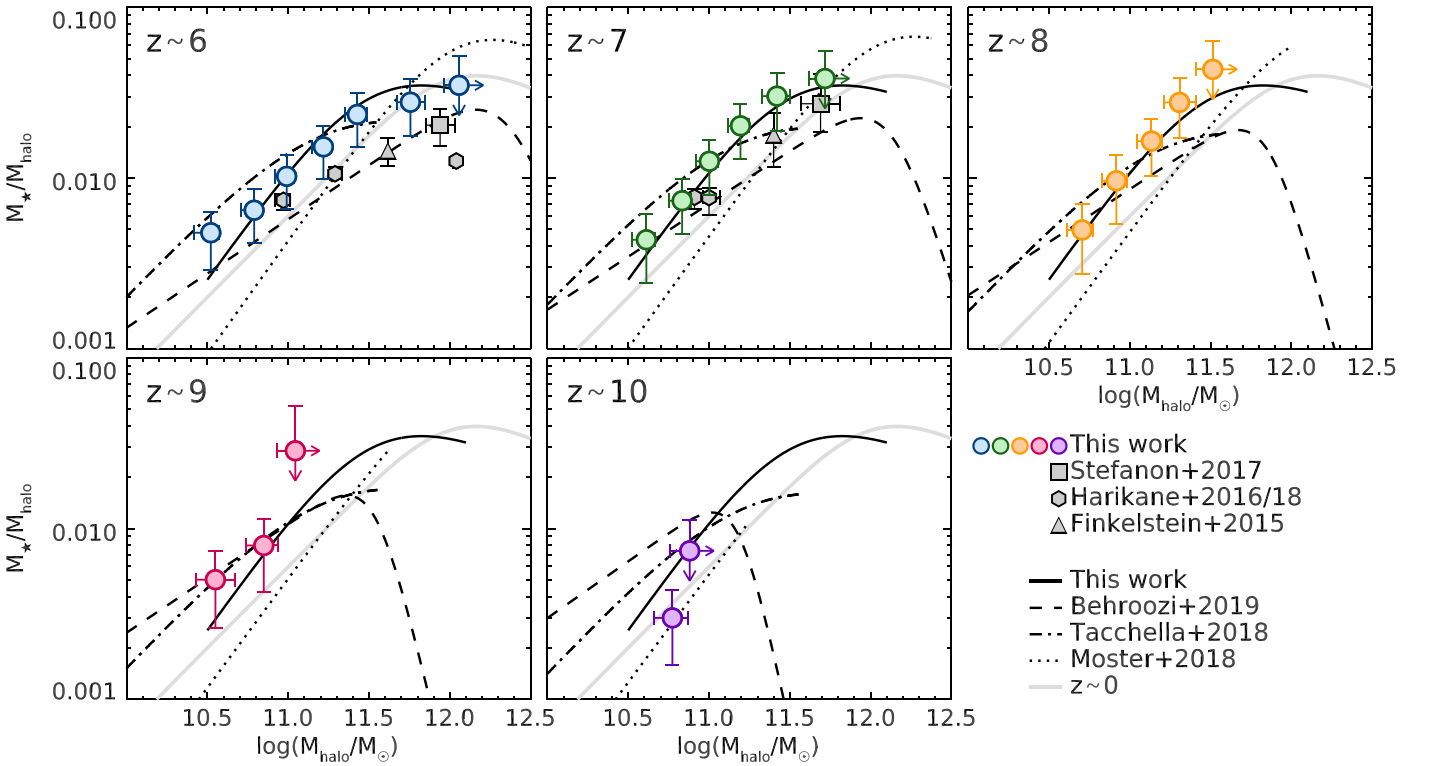
Figure 13. Comparison of the stellar-to-halo mass ratios estimated in this study to previous observational estimates of Finkelstein et al. (2015b), Harikane et al. (2018) and Stefanon et al. (2017) (symbols as per the bottom right legend). Also presented is our redshift-independent best-fitting relation and the redshift-evolving stellar-to-halo mass relations from the semi-analytic model of Behroozi et al. (2019), the moderately evolving SHMR of Moster et al. (2018), and the marginally evolving SHMR from the semi-analytic models of Tacchella et al. (2018) (legend at the bottom right). The gray solid curve corresponds to the $z \sim 0$ SHMR from Behroozi et al. (2013), which we display as reference. We used the relations derived in Appendix D to convert the halo mass estimates of Finkelstein et al. (2015b) and the curves of Tacchella et al. (2018) from a WMAP7 cosmology into one consistent with that of Planck Collaboration et al. (2016). The solid points with arrows mark those halo mass measurements whose lower uncertainty remained undefined because of the limited range available for v_{acc}. The broad agreement with the predictions with constant SHMR (see text) provide further support to a nonevolving SHMR in the early universe.

Table 7
Dark Matter Halo Masses and Stellar-to-halo Mass Ratios

Redshift	$\log(\mathcal{M}_\star/\mathcal{M}_\odot)$[a]	$\log(\mathcal{M}_h/\mathcal{M}_\odot)$[b]	$\mathcal{M}_\star/\mathcal{M}_h$[c]	$\log(\text{cum. den.}/\text{Mpc}^{-3})$[d]	$\log(v_{acc}/\text{km s}^{-1})$[e]
5.80	8.20 ± 0.14	$10.52^{+0.05}_{-0.10}$	$4.8^{+1.6}_{-1.9} \times 10^{-3}$	$-2.19^{+0.04}_{-0.04}$	$2.01^{+0.01}_{-0.01}$
	8.60 ± 0.14	$10.79^{+0.05}_{-0.08}$	$6.5^{+2.1}_{-2.3} \times 10^{-3}$	$-2.62^{+0.03}_{-0.03}$	$2.10^{+0.01}_{-0.01}$
	9.00 ± 0.14	$10.99^{+0.05}_{-0.07}$	$10.^{+3.}_{-4.} \times 10^{-3}$	$-2.97^{+0.05}_{-0.05}$	$2.16^{+0.01}_{-0.01}$
	9.40 ± 0.14	$11.22^{+0.05}_{-0.07}$	$15.^{+5.}_{-5.} \times 10^{-3}$	$-3.40^{+0.05}_{-0.05}$	$2.24^{+0.01}_{-0.01}$
	9.80 ± 0.14	$11.43^{+0.06}_{-0.08}$	$24.^{+8.}_{-8.} \times 10^{-3}$	$-3.85^{+0.12}_{-0.13}$	$2.31^{+0.02}_{-0.02}$
	10.20 ± 0.14	$11.76^{+0.09}_{-0.08}$	$28.^{+10.}_{-10.} \times 10^{-3}$	$-4.65^{+0.22}_{-0.31}$	$2.43^{+0.04}_{-0.03}$
	10.60 ± 0.14	>11.97	$<52 \times 10^{-3}$	<-5.17	>2.50
6.79	8.25 ± 0.17	$10.61^{+0.05}_{-0.09}$	$4.3^{+1.8}_{-1.9} \times 10^{-3}$	$-2.69^{+0.06}_{-0.06}$	$2.07^{+0.01}_{-0.01}$
	8.70 ± 0.14	$10.83^{+0.05}_{-0.08}$	$7.4^{+2.5}_{-2.7} \times 10^{-3}$	$-3.11^{+0.05}_{-0.05}$	$2.14^{+0.01}_{-0.01}$
	9.10 ± 0.14	$11.00^{+0.05}_{-0.08}$	$13.^{+4.}_{-5.} \times 10^{-3}$	$-3.45^{+0.07}_{-0.07}$	$2.20^{+0.01}_{-0.01}$
	9.50 ± 0.14	$11.19^{+0.05}_{-0.08}$	$20.^{+7.}_{-7.} \times 10^{-3}$	$-3.87^{+0.09}_{-0.09}$	$2.27^{+0.01}_{-0.01}$
	9.90 ± 0.14	$11.42^{+0.08}_{-0.09}$	$30.^{+11.}_{-11.} \times 10^{-3}$	$-4.42^{+0.19}_{-0.25}$	$2.34^{+0.04}_{-0.02}$
	10.30 ± 0.14	>11.62	$<55 \times 10^{-3}$	<-4.93	>2.41
7.68	8.40 ± 0.17	$10.71^{+0.07}_{-0.10}$	$5.0^{+2.1}_{-2.2} \times 10^{-3}$	$-3.33^{+0.10}_{-0.10}$	$2.13^{+0.02}_{-0.02}$
	8.90 ± 0.17	$10.92^{+0.07}_{-0.09}$	$9.6^{+4.1}_{-4.2} \times 10^{-3}$	$-3.80^{+0.13}_{-0.14}$	$2.20^{+0.02}_{-0.02}$
	9.35 ± 0.14	$11.13^{+0.07}_{-0.09}$	$16.^{+6.}_{-6.} \times 10^{-3}$	$-4.31^{+0.16}_{-0.16}$	$2.27^{+0.02}_{-0.02}$
	9.75 ± 0.14	$11.31^{+0.10}_{-0.10}$	$28.^{+11.}_{-11.} \times 10^{-3}$	$-4.83^{+0.29}_{-0.44}$	$2.34^{+0.05}_{-0.04}$
	10.15 ± 0.14	>11.41	$<63 \times 10^{-3}$	<-5.10	>2.37
8.90	8.25 ± 0.17	$10.55^{+0.12}_{-0.12}$	$5.0^{+2.4}_{-2.4} \times 10^{-3}$	$-3.87^{+0.31}_{-0.45}$	$2.13^{+0.06}_{-0.05}$
	8.75 ± 0.17	$10.85^{+0.09}_{-0.11}$	$8.0^{+3.5}_{-3.7} \times 10^{-3}$	$-4.58^{+0.22}_{-0.27}$	$2.23^{+0.03}_{-0.03}$
	9.50 ± 0.34	>10.93	$<55 \times 10^{-3}$	<-4.86	>2.26
9.75	8.25 ± 0.17	$10.77^{+0.10}_{-0.11}$	$3.0^{+1.4}_{-1.4} \times 10^{-3}$	$-4.96^{+0.34}_{-0.46}$	$2.22^{+0.05}_{-0.04}$
	8.75 ± 0.17	>10.76	$<11.2 \times 10^{-3}$	<-4.91	>2.22

Notes. Upper/lower limits are 2σ.
[a] Central value of the stellar mass bin adopted for our SMF estimates. The uncertainty corresponds to $\pm 34\%$ the width of the mass bin.
[b] Halo mass recovered through our abundance matching procedure.
[c] Stellar-to-halo mass ratio. Uncertainties correspond to the propagation of the uncertainties in the stellar and halo masses.
[d] Cumulative density adopted for the abundance matching, computed for the central mass of each stellar mass bin.
[e] Accretion velocity of the dark matter halos for the cumulative density in adjacent column (d).

there are no other estimates to date of the SHMRs at $z \sim 8$, $z \sim 9$, and $z \sim 10$.

Our estimates are consistent with those of Stefanon et al. (2017) at $<1\sigma$ and of Finkelstein et al. (2015b) at $\gtrsim 1\sigma$, both of which are based on abundance matching techniques, and with those of Harikane et al. (2018) for $\mathcal{M}_{halo} < 10^{11}\mathcal{M}_\odot$ at $\sim 1\sigma$, which were derived from clustering measurements. In the same panels, we also present SHMR from three recent models, which use different assumptions on the evolution of the SHMR with cosmic time: Tacchella et al. (2018) assumed the SHMR to be approximately constant above $z \sim 4$; Moster et al. (2018) linked the star formation rate to the halo accretion rate through a redshift-dependent parametric baryon conversion efficiency (see also Sun & Furlanetto 2016 and Furlanetto et al. 2017 for a similar approach); finally, Behroozi et al. (2019) did not introduce any correlation between the evolution of the dark matter halos and (baryonic) galaxy assembly, finding an SHMR increasing with redshift (see also Behroozi et al. 2013, but see Zhu et al. 2020). Figure 13 shows that our measurements are generally in good agreement with the predictions of Tacchella et al. (2018) over the full redshift range probed here and with those of Behroozi et al. (2019) at $z \sim 8$–10, further supporting a nonevolving SHMR in the early universe.

8. Summary and Conclusions

The new deep, wide GREATS IRAC data set, combined with a much larger Hubble sample, has allowed us to derive statistically robust SMFs from ~ 800 galaxies at redshifts between $z \sim 6$ and $z \sim 10$. The comprehensive catalog of Lyman-break galaxies (LBG) was assembled from the source lists of Bouwens et al. (2015, 2016b, 2019) and Oesch et al. (2018) over the GOODS, the HUDF/XDF, and all five CANDELS fields. Our stellar mass samples are distinctive compared to previous studies at similar redshifts due to our use of (1) a much deeper wide area (~ 200 hr) Spitzer/IRAC imaging data set at 3.6 μm and 4.5 μm from the GOODS Re-ionization Era Wide-Area Treasury from Spitzer (GREATS) program (PI: I. Labbé—Stefanon et al. 2021b) and (2) a $3\times$ larger search volume than previous HST-based galaxy SMFs. These new deep Spitzer data greatly increased the number and fraction of IRAC-detected sources from the UV catalogs. For example, $>50\%$ of the sources with stellar masses $\mathcal{M}_\star > 10^8\mathcal{M}_\odot$ showed $\geqslant 2\,\sigma$ detection in the rest-frame optical. Constraining the UV-selected sources with a large fraction of IRAC measurements significantly increased the robustness of our stellar mass measurements.

Our SMFs were derived using the V_{max} method of Avni & Bahcall (1980) on individual sources. Schechter fits to the $z \sim 6$–8 SMFs suggest a nonevolving low-mass end slope $\alpha \sim -1.8$, broadly consistent with previous estimates. The χ^2 contours indicate that the SMFs evolve in both the characteristic stellar mass $\mathcal{M}^*$ and the number density normalization factor ϕ^*. The SMD increases by $\sim 1000 \times$ in the 0.5 Gyr between $z \sim 10$ and $z \sim 6$, with an evolution qualitatively consistent with that of the star formation rate density (see, e.g., Oesch et al. 2018). This rapid growth during the first Gyr in just 500 Myr since $z \sim 10$ contrasts with the further, and slower, $\sim 100 \times$ increase over the next 13 Gyr to $z \sim 0$.

We performed abundance matching of our SMFs to the Bolshoi–Planck simulation (Klypin et al. 2016). Our analysis shows that the SMD follows the growth rate of the halo mass density from $z \sim 10$ to $z \sim 3$–4. In particular, a fit to the ratio between the dark-matter halo mass density and the stellar mass density at $z \geqslant 4$ gives:

$$\log(\rho_h/\rho_{\mathcal{M}_\star}) = (1.976 \pm 0.104) + (0.037 \pm 0.041) \times (z - 7).$$

$$(8)$$

Remarkably, we find no evidence of evolution in the SHMRs from $z \sim 10$ to $z \sim 6$ for galaxies in the $10^8 < \mathcal{M}_\star/\mathcal{M}_\odot \lesssim 10^{10}$ stellar mass range. This is even more remarkable given the three orders-of-magnitude increase in the SMD in the 500 Myr from $z \sim 10$ to $z \sim 6$ noted above. Our results at the earliest times fit well with those found previously for later times $z \leqslant 6$. Our results furthermore indicate at most a marginal evolution of the star formation efficiency at these early epochs, nicely consistent with many recent empirical models (e.g., Tacchella et al. 2018; Park et al. 2019).

In the near future, the JWST will significantly increase the sensitivity of the flux measurements at 3–5 μm. Source confusion, which can be challenging to overcome with the Spitzer/IRAC data, will be much less of a concern due to an impressive ~ 10–15$\times$ reduction in the PSF FWHM at 3–5 μm. The substantially improved flux measurements at longer wavelengths will also come with improvements in the efficiency with which sources are selected. This will not only improve stellar masses and SMF estimates but also the measurement of halo masses from clustering analyses to $z \sim 10$ (e.g., Endsley et al. 2020).

While our new Hubble and Spitzer SMF results have yielded striking insights into the lack of significant changes in the SHMRs and in the star formation efficiency in the first Gyr from $z \sim 10$ to $z \sim 6$ when truly dramatic growth is occurring in the SMD, JWST is poised to take us even further. JWST will provide more detailed insights and verification at $z \leqslant 10$, but, crucially, will reveal what happens to the star formation efficiency prior to $z \sim 10$, into the epoch of the "first galaxies" during the first 500 Myr of cosmic time.

Appendix A
Completeness Estimate

We assessed the statistical effects of our IRAC selection on our sample through a Monte Carlo simulation. This consisted of adding synthetic sources to the GREATS 3.6 μm and 4.5 μm mosaics and recovering their flux density and contamination using MOPHONGO. The synthetic sources were added at random locations across the 3.6 μm-band mosaic and then at the same locations when adding sources in the 4.5 μm band. This procedure was repeated over a suitable range of flux densities. We estimated the fraction of sources excluded because of high neighbor contamination by applying the same selection criteria adopted for the main sample assuming a flat f_ν SED. To evaluate the effectiveness of the estimated correction, we computed the UV luminosity function from the HST sources excluding those with neighbor contamination in the IRAC bands at $z \sim 6$, 7, and 8 using the V_{max} formalism (Avni & Bahcall 1980) and weighting the volumes associated to each source by the estimated correction. Figure 14 presents the result of this exercise. Our completeness corrections are clearly larger for fainter sources in our samples. This is a result of the fact that, for fainter sources, even a small contribution of light at 3.6 μm and 4.5 μm from their neighbors is sufficient to satisfy the 65% IRAC contamination threshold for exclusion from our sample. Comparison of our UV LFs to those of Bouwens et al. (2015) show a good agreement over the full range of luminosities and for all redshifts. However, the median of the corrections become very large ($>10\times$) for the faintest sources $M_{UV} \gtrsim -16.75, -17.25$, and ~ -17.5 mag in our $z \sim 6$, 7, and ~ 8 selections, respectively, making the associated volume densities more uncertain. For this reason, in our analysis we exclude those measurements potentially affected by this aspect.
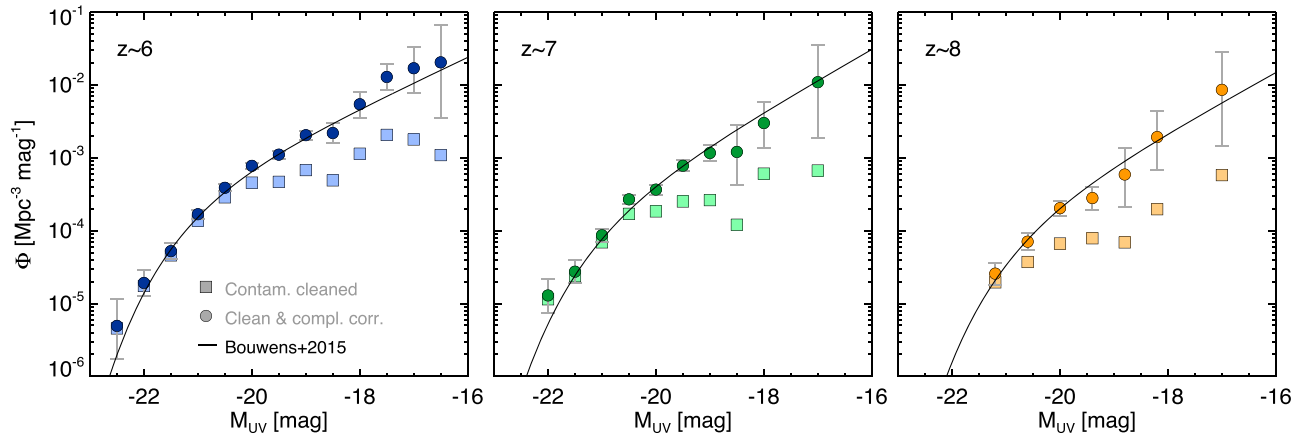
Figure 14. Effectiveness of recovering the HST UV luminosity distribution after excluding sources from the HST sample with >65% contamination by neighbors in the IRAC 3.6 μm and 4.5 μm bands. Each panel refers to a specific redshift bin, as labeled in the top left corner. The filled square symbols represent the UV luminosity function computed after cleaning the sample from the contaminated sources, while the filled circles mark the volume density obtained after applying the completeness corrections computed through our Monte Carlo simulation (see Section 2 for details). The solid black curve corresponds to the Schechter parameterization of Bouwens et al. (2015), adopted as reference. The small IRAC flux densities of faint sources imply lower contributions from the neighboring objects are sufficient to satisfy the contamination criteria, making completeness corrections increasingly large for faint sources. Our completeness estimates allow us to recover the UV LF very well to $M_{\rm UV} \gtrsim -17.0$. However, the median corrections are >10× for $M_{\rm UV} \sim -16.75, -17.25$, and ~-17.5 at $z \sim 6, 7$, and ~8, respectively, making the corresponding volume densities at low luminosities highly uncertain.

Appendix B
Comparison of Stellar Mass Estimates from Our Different Methods

In Figure 15, we compare the stellar mass estimates of the full sample at $z \sim 6$–8 estimated using the methods described in Sections 3.1–3.3, as a function of the UV slope and UV luminosity, in the three redshift bins. The stellar mass estimates from the updated IRAC bands for sources detected at >3σ significance in both IRAC bands are on average consistent with those obtained with the SED analysis on the original photometry. Because the systematic differences are marginal and within the 1σ dispersions (see Figure 15), we concluded that the new set of stellar masses can confidently be used for those sources with <2σ significance in at least one of the two IRAC bands for the $z \sim 6, 7$, and 8 samples.
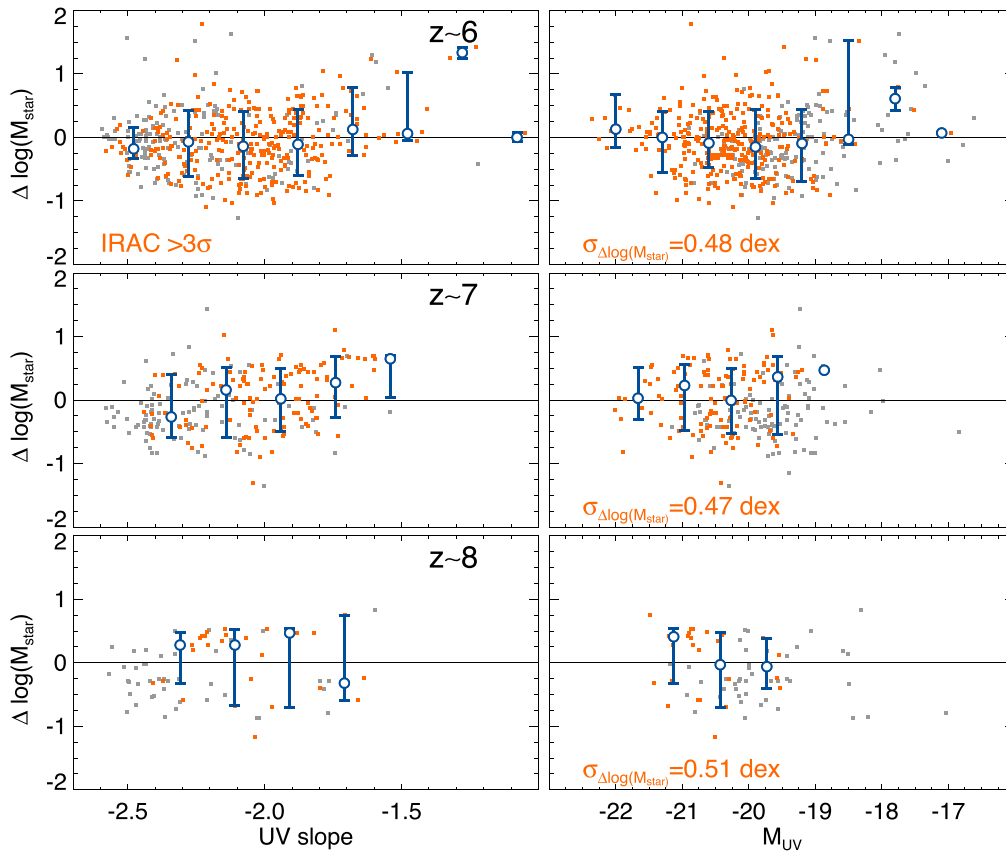
Figure 15. Comparison between the stellar mass measurements obtained with SED templates that included emission by nebular continuum and lines ($\equiv M_{\mathrm{star,full}}$) and those for which the rest-frame optical free-from-emission-line contribution is reconstructed using the relation between the $H - [3.6]$ color and the UV slope ($\equiv M_{\mathrm{star,}}$ $_{\mathrm{H36}}$) of Stefanon et al. (2021a). From top to bottom, the panels refer to the $z \sim 6$, $z \sim 7$, and $z \sim 8$ redshift bins. For each redshift bin, the left panel presents $\Delta \log(M_{\mathrm{star}}) \equiv \log(M_{\mathrm{star,full}}) - \log(M_{\mathrm{star,H36}})$ as a function of the UV slope, while the panels on the right present $\Delta \log(M_{\mathrm{star}})$ as a function of the UV luminosity M_{UV}. Grey points correspond to the full sample, while orange points mark those sources with higher significance in the two IRAC bands, as indicated by the label in the top left panel. Finally, the blue points with error bars correspond to the median and 68% confidence interval of the sources with higher IRAC significance. The relative consistency between our stellar mass estimates made using the full SED information for IRAC-detected sources and estimates made relying on the UV slope information alone (exploiting a relationship we found in Stefanon et al. 2021a) gives us confidence in using this prescription for sources lacking clear 2σ detections with IRAC.

Appendix C
Stellar Mass-to-light Ratios

In Figure 16, we compare our estimates of the $\mathcal{M}_\star - M_{\mathrm{UV}}$ relationship at $z \sim 6$, 7, 8, and 9 to those at similar redshifts from recent determinations (Duncan et al. 2014; Song et al. 2016; Bhatawdekar et al. 2019; Kikuchihara et al. 2020). Our recovered slopes are in general consistent with previous determinations. Interestingly, at $z \sim 6$, 7, and 8, our stellar masses seem to be $\sim$0.2–0.3 dex lower than the average of previous estimates. At $z \sim 9$, this difference increases to $\sim$0.5–1.0 dex. This difference could, at least in part, be due to the strong emission lines recovered from our improved IRAC colors, which have higher S/N than in previous studies, implying younger stellar populations and lower $\mathcal{M}_\star / L_{\mathrm{UV}}$ ratios. The use of the higher S/N GREATS data suggests that our results are likely to be representative of the true values.
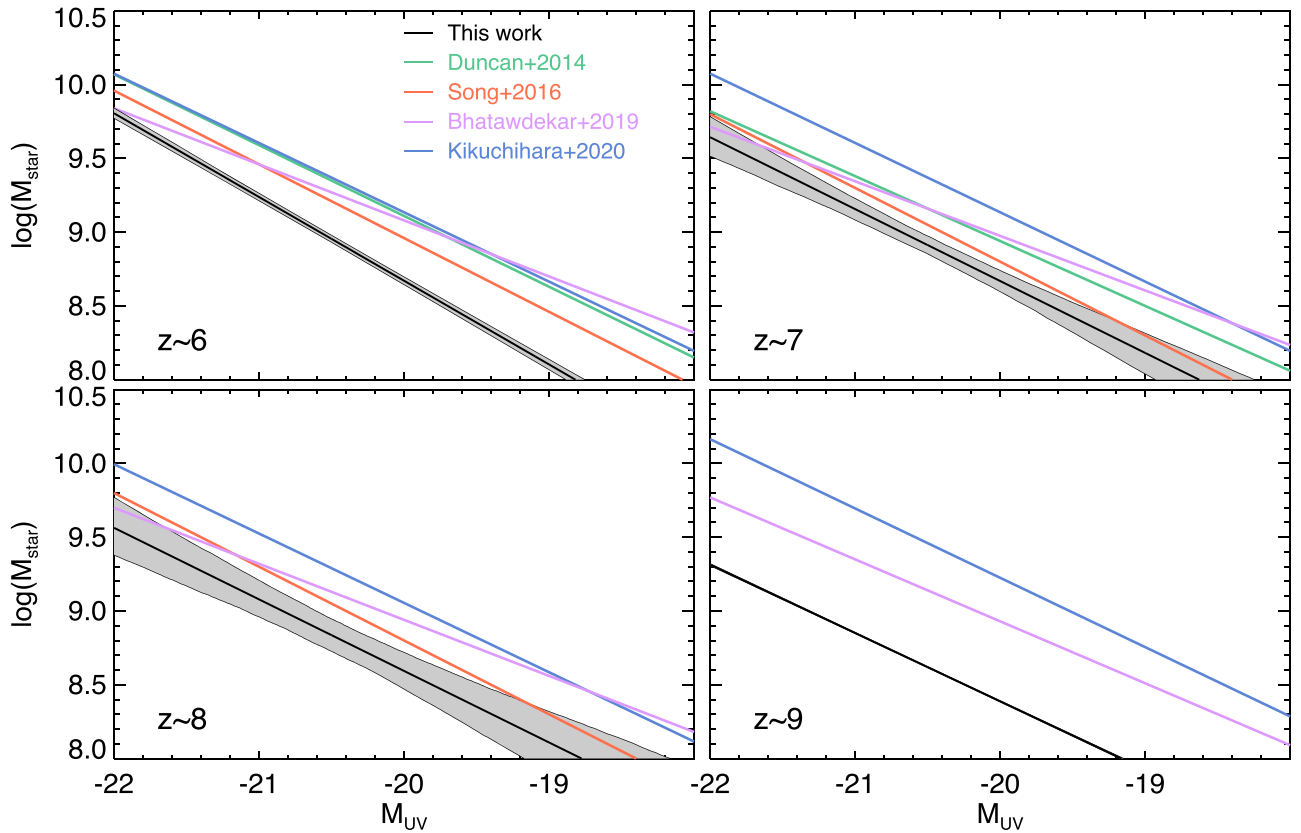
Figure 16. Comparison of our $\mathcal{M}_\star - M_{UV}$ relation to some of the most recent estimates in the literature, as indicated by the legend in the top left panel. The gray-shaded areas encompass the 68% confidence interval from our best-fit values. The tight relationship at $z \sim 9$ is likely a consequence of similar SEDs resulting from our procedure of reconstructing the flux densities in the IRAC bands discussed in Section 3.4.

Appendix D
Conversion of SHMR Based on WMAP7 Cosmology into Planck Cosmology

In Section 7.3.2, we discuss our measurements of the SHMR and compare them to previous observational results and model expectations. Our SHMR estimates and those of Harikane et al. (2016, 2018), Moster et al. (2018), and Behroozi et al. (2019) were obtained assuming a cosmology consistent with the Planck Collaboration et al. (2016) results, whereas the SHMR estimates of Finkelstein et al. (2015b) and Tacchella et al. (2018) are based on the WMAP7 cosmology (Komatsu et al. 2011). For illustrative purposes, in the left panel of Figure 17 we compare the HMF at $z = 6$ and $z = 8$ from the two cosmologies. Specifically, we adopted the Behroozi et al. (2013) HMF generated by the HMFCALC tool

(Murray et al. 2013). When WMAP7 HMFs are adopted for abundance matching procedures, the systematic differences in the volume densities between the two cosmologies translate into ~ 0.05–0.06 dex lower halo masses and $\sim 15\%$ higher SHMR for WMAP7-based observables compared to Planck-based ones.

To allow for a consistent comparison of all of these estimates, we matched the cumulative volume density of dark matter halos in the two cosmologies and computed the ratio of the corresponding halo masses. The multiplicative factors we used to convert the halo masses presented in Finkelstein et al. (2015b) and Tacchella et al. (2018) to Planck-based halo masses are presented in the right panel of Figure 17. These factors depend on redshift but are approximately independent of the halo mass within the halo mass range considered in our work ($10^{10.5}$–$10^{12} \mathcal{M}_\odot$).
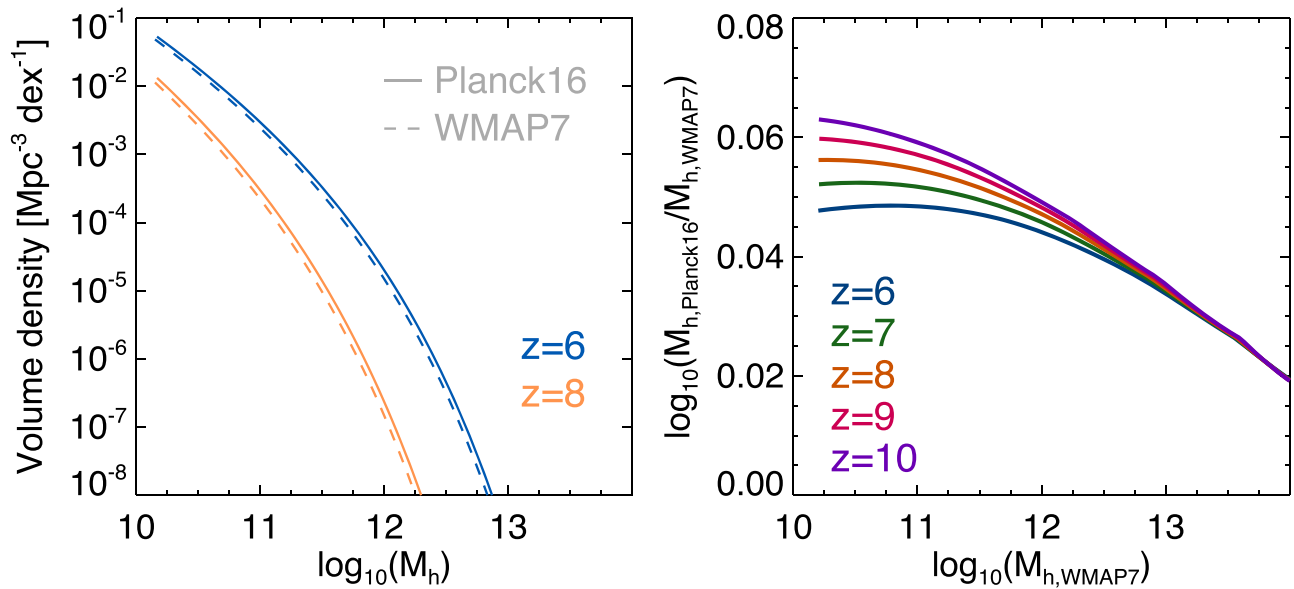
Figure 17. (Left): HMF at $z = 6$ (blue curves) and $z = 8$ (orange) from the Planck Collaboration et al. (2016) (solid curves) and WMAP7 (Komatsu et al. 2011) cosmology. (Right): Ratio (in log scale) between the halo masses from the WMAP 7 (Komatsu et al. 2011) cosmology to those from the Planck Collaboration et al. (2016) cosmology for the five redshift bins considered in this work, and derived after matching the cumulative number densities of the corresponding halo mass functions. The correction factor depends on the specific redshift but is approximately independent of the halo mass within the halo mass range considered in our work ($10^{10.5}$–$10^{12} \mathcal{M}_\odot$).

ORCID iDs

Mauro Stefanon https://orcid.org/0000-0001-7768-5309
Rychard J. Bouwens https://orcid.org/0000-0002-4989-2471
Garth D. Illingworth https://orcid.org/0000-0002-8096-2837
Valentino Gonzalez https://orcid.org/0000-0002-3120-0510
Pascal A. Oesch https://orcid.org/0000-0001-5851-6649

References

Alcalde Pampliega, B., Pérez-González, P. G., Barro, G., et al. 2019, ApJ, 876, 135
Anders, P., & Fritze-v. Alvensleben, U. 2003, A&A, 401, 1063
Arnouts, S., Walcher, C. J., Le Fèvre, O., et al. 2007, A&A, 476, 137
Ashby, M. L. N., Caputi, K. I., Cowley, W., et al. 2018, ApJS, 237, 39
Ashby, M. L. N., Willner, S. P., Fazio, G. G., et al. 2013, ApJ, 769, 80
Ashby, M. L. N., Willner, S. P., Fazio, G. G., et al. 2015, ApJS, 218, 33
Avni, Y., & Bahcall, J. N. 1980, ApJ, 235, 694
Baugh, C. M. 2006, RPPh, 69, 3101
Beckwith, S. V. W., Stiavelli, M., Koekemoer, A. M., et al. 2006, AJ, 132, 1729
Behroozi, P., Wechsler, R. H., Hearin, A. P., & Conroy, C. 2019, MNRAS, 488, 3143
Behroozi, P. S., Wechsler, R. H., & Conroy, C. 2013, ApJ, 770, 57
Bhatawdekar, R., & Conselice, C. J. 2021, ApJ, 909, 144
Bhatawdekar, R., Conselice, C. J., Margalef-Bentabol, B., & Duncan, K. 2019, MNRAS, 486, 3805
Bhowmick, A. K., Di Matteo, T., Feng, Y., & Lanusse, F. 2018, MNRAS, 474, 5393
Bhowmick, A. K., Somerville, R. S., Di Matteo, T., et al. 2020, MNRAS, 496, 754
Bielby, R., Hudelot, P., McCracken, H. J., et al. 2012, A&A, 545, A23
Bouwens, R., González-López, J., Aravena, M., et al. 2020, ApJ, 902, 112
Bouwens, R. J., Aravena, M., Decarli, R., et al. 2016a, ApJ, 833, 72
Bouwens, R. J., Bradley, L., Zitrin, A., et al. 2014a, ApJ, 795, 126
Bouwens, R. J., Illingworth, G. D., Labbe, I., et al. 2011a, Natur, 469, 504
Bouwens, R. J., Illingworth, G. D., Oesch, P. A., et al. 2011b, ApJ, 737, 90
Bouwens, R. J., Illingworth, G. D., Oesch, P. A., et al. 2014b, ApJ, 793, 115
Bouwens, R. J., Illingworth, G. D., Oesch, P. A., et al. 2015, ApJ, 803, 34
Bouwens, R. J., Oesch, P. A., Illingworth, G. D., et al. 2013, ApJL, 765, L16
Bouwens, R. J., Oesch, P. A., Illingworth, G. D., Ellis, R. S., & Stefanon, M. 2017, ApJ, 843, 129
Bouwens, R. J., Oesch, P. A., Labbé, I., et al. 2016b, ApJ, 830, 67
Bouwens, R. J., Oesch, P. A., Stefanon, M., et al. 2021, arXiv:2102.07775
Bouwens, R. J., Stefanon, M., Oesch, P. A., et al. 2019, ApJ, 880, 25
Brammer, G. B., van Dokkum, P. G., & Coppi, P. 2008, ApJ, 686, 1503
Bruzual, G., & Charlot, S. 2003, MNRAS, 344, 1000
Calvi, V., Trenti, M., Stiavelli, M., et al. 2016, ApJ, 817, 120
Calzetti, D., Armus, L., Bohlin, R. C., et al. 2000, ApJ, 533, 682
Campbell, D., van den Bosch, F. C., Padmanabhan, N., et al. 2018, MNRAS, 477, 359
Caputi, K. I., Cirasuolo, M., Dunlop, J. S., et al. 2011, MNRAS, 413, 162
Caputi, K. I., Deshmukh, S., Ashby, M. L. N., et al. 2017, ApJ, 849, 45
Caputi, K. I., Dunlop, J. S., McLure, R. J., et al. 2012, ApJL, 750, L20
Caputi, K. I., Ilbert, O., Laigle, C., et al. 2015, ApJ, 810, 73
Castellano, M., Amorín, R., Merlin, E., et al. 2016, A&A, 590, A31
Ceverino, D., Klessen, R. S., & Glover, S. C. O. 2018, MNRAS, 480, 4842
Chabrier, G. 2003, PASP, 115, 763
Coe, D., Zitrin, A., Carrasco, M., et al. 2013, ApJ, 762, 32
Conroy, C., Wechsler, R. H., & Kravtsov, A. V. 2006, ApJ, 647, 201
Davidzon, I., Ilbert, O., Laigle, C., et al. 2017, A&A, 605, A70
Davis, M., Guhathakurta, P., Konidaris, N. P., et al. 2007, ApJL, 660, L1
Dayal, P., & Ferrara, A. 2018, PhR, 780, 1
De Barros, S., Oesch, P. A., Labbé, I., et al. 2019, MNRAS, 489, 2355
De Barros, S., Pentericci, L., Vanzella, E., et al. 2017, A&A, 608, A123
Driver, S. P., & Robotham, A. S. G. 2010, MNRAS, 407, 2131
Duncan, K., & Conselice, C. J. 2015, MNRAS, 451, 2030
Duncan, K., Conselice, C. J., Mortlock, A., et al. 2014, MNRAS, 444, 2960
Dunlop, J. S., Abraham, R. G., Ashby, M. L. N., et al. 2021, JWST Proposal
Dunlop, J. S., McLure, R. J., Biggs, A. D., et al. 2017, MNRAS, 466, 861
Dunlop, J. S., Rogers, A. B., McLure, R. J., et al. 2013, MNRAS, 432, 3520
Durkalec, A., Le Fèvre, O., de la Torre, S., et al. 2015, A&A, 576, L7
Eldridge, J. J., Stanway, E. R., Xiao, L., et al. 2017, PASA, 34, e058
Ellis, R. S., McLure, R. J., Dunlop, J. S., et al. 2013, ApJL, 763, L7
Endsley, R., Behroozi, P., Stark, D. P., et al. 2020, MNRAS, 493, 1178
Endsley, R., Stark, D. P., Chevallard, J., & Charlot, S. 2021, MNRAS, 500, 5229
Eyles, L. P., Bunker, A. J., Ellis, R. S., et al. 2007, MNRAS, 374, 910
Faisst, A. L., Capak, P., Hsieh, B. C., et al. 2016, ApJ, 821, 122
Faisst, A. L., Capak, P. L., Emami, N., Tacchella, S., & Larson, K. L. 2019, ApJ, 884, 133
Faisst, A. L., Schaerer, D., Lemaux, B. C., et al. 2020, ApJS, 247, 61

Fall, S. M., & Efstathiou, G. 1980, MNRAS, 193, 189
Fazio, G. G., Hora, J. L., Allen, L. E., et al. 2004, ApJS, 154, 10
Ferland, G. J., Chatzikos, M., Guzmán, F., et al. 2017, RMxAA, 53, 385
Fialkov, A., & Loeb, A. 2015, ApJ, 806, 256
Finkelstein, S. L., Papovich, C., Dickinson, M., et al. 2013, Natur, 502, 524
Finkelstein, S. L., Papovich, C., Pirzkal, N., et al. 2021, JWST Proposal
Finkelstein, S. L., Papovich, C., Salmon, B., et al. 2012, ApJ, 756, 164
Finkelstein, S. L., Ryan, R. E., Jr., Papovich, C., et al. 2015a, ApJ, 810, 71
Finkelstein, S. L., Song, M., Behroozi, P., et al. 2015b, ApJ, 814, 95
Fontana, A., Salimbeni, S., Grazian, A., et al. 2006, A&A, 459, 745
Fudamoto, Y., Oesch, P. A., Schouws, S., et al. 2020, Natur, 597, 489
Furlanetto, S. R., Mirocha, J., Mebane, R. H., & Sun, G. 2017, MNRAS, 472, 1576
Furtak, L. J., Atek, H., Lehnert, M. D., Chevallard, J., & Charlot, S. 2021, MNRAS, 501, 1568
Gallazzi, A., Brinchmann, J., Charlot, S., & White, S. D. M. 2008, MNRAS, 383, 1439
Gehrels, N. 1986, ApJ, 303, 336
Giavalisco, M., Ferguson, H. C., Koekemoer, A. M., et al. 2004, ApJL, 600, L93
Girelli, G., Pozzetti, L., Bolzonella, M., et al. 2020, A&A, 634, A135
González, V., Bouwens, R. J., Labbé, I., et al. 2012, ApJ, 755, 148
González, V., Labbé, I., Bouwens, R. J., et al. 2011, ApJL, 735, L34
Grazian, A., Fontana, A., Santini, P., et al. 2015, A&A, 575, A96
Grogin, N. A., Kocevski, D. D., Faber, S. M., et al. 2011, ApJS, 197, 35
Gruppioni, C., Béthermin, M., Loiacono, F., et al. 2020, A&A, 643, A8
Harikane, Y., Ouchi, M., Ono, Y., et al. 2016, ApJ, 821, 123
Harikane, Y., Ouchi, M., Ono, Y., et al. 2018, PASJ, 70, S11
Hashimoto, T., Laporte, N., Mawatari, K., et al. 2018, Natur, 557, 392
Hoag, A., Bradač, M., Brammer, G., et al. 2018, ApJ, 854, 39
Huang, J.-S., Zheng, X. Z., Rigopoulou, D., et al. 2011, ApJL, 742, L13
Hutter, A., Dayal, P., Yepes, G., et al. 2021, MNRAS, 503, 3698
Ilbert, O., McCracken, H. J., Le Fèvre, O., et al. 2013, A&A, 556, A55
Illingworth, G. D., Magee, D., Oesch, P. A., et al. 2013, ApJS, 209, 6
Inoue, A. K. 2011, MNRAS, 415, 2920
Kajisawa, M., Ichikawa, T., Tanaka, I., et al. 2009, ApJ, 702, 1393
Kartaltepe, J., Casey, C. M., Bagley, M., et al. 2021, JWST Proposal
Kikuchihara, S., Ouchi, M., Ono, Y., et al. 2020, ApJ, 893, 60
Klypin, A., Yepes, G., Gottlöber, S., Prada, F., & Heß, S. 2016, MNRAS, 457, 4340
Koekemoer, A. M., Faber, S. M., Ferguson, H. C., et al. 2011, ApJS, 197, 36
Komatsu, E., Smith, K. M., Dunkley, J., et al. 2011, ApJS, 192, 18
Kravtsov, A. V., Berlind, A. A., Wechsler, R. H., et al. 2004, ApJ, 609, 35
Kriek, M., van Dokkum, P. G., Labbé, I., et al. 2009, ApJ, 700, 221
Labbe, I., Bezanson, R., Atek, H., et al. 2021, WST Proposal
Labbé, I., Bouwens, R., Illingworth, G. D., & Franx, M. 2006, ApJL, 649, L67
Labbé, I., González, V., Bouwens, R. J., et al. 2010a, ApJL, 716, L103
Labbé, I., González, V., Bouwens, R. J., et al. 2010b, ApJL, 708, L26
Labbé, I., Oesch, P. A., Bouwens, R. J., et al. 2013, ApJL, 777, L19
Labbé, I., Oesch, P. A., Illingworth, G. D., et al. 2015, ApJS, 221, 23
Lam, D., Bouwens, R. J., Coe, D., et al. 2019, arXiv:1903.08177
Lawrence, A., Warren, S. J., Almaini, O., et al. 2007, MNRAS, 379, 1599
Lee, K.-S., Ferguson, H. C., Wiklind, T., et al. 2012, ApJ, 752, 66
Legrand, L., McCracken, H. J., Davidzon, I., et al. 2019, MNRAS, 486, 5468
Leja, J., Johnson, B. D., Conroy, C., et al. 2019, ApJ, 877, 140
Li, C., & White, S. D. M. 2009, MNRAS, 398, 2177
Lima, M., Jain, B., & Devlin, M. 2010, MNRAS, 406, 2352
Lotz, J. M., Koekemoer, A., Coe, D., et al. 2017, ApJ, 837, 97
Lower, S., Narayanan, D., Leja, J., et al. 2020, ApJ, 904, 33
Ma, X., Hopkins, P. F., Garrison-Kimmel, S., et al. 2018, MNRAS, 478, 1694
Madau, P., & Dickinson, M. 2014, ARA&A, 52, 415
Marchesini, D., van Dokkum, P. G., Förster Schreiber, N. M., et al. 2009, ApJ, 701, 1765
Mashian, N., Oesch, P. A., & Loeb, A. 2016, MNRAS, 455, 2101
Mason, C. A., Trenti, M., & Treu, T. 2015a, ApJ, 813, 21
Mason, C. A., Treu, T., Schmidt, K. B., et al. 2015b, ApJ, 805, 79
McLeod, D. J., McLure, R. J., & Dunlop, J. S. 2016, MNRAS, 459, 3812
McLeod, D. J., McLure, R. J., Dunlop, J. S., et al. 2021, MNRAS, 503, 4413
McLure, R. J., Dunlop, J. S., Bowler, R. A. A., et al. 2013, MNRAS, 432, 2696
Merlin, E., Amorín, R., Castellano, M., et al. 2016, A&A, 590, A30
Michałowski, M. J., Hayward, C. C., Dunlop, J. S., et al. 2014, A&A, 571, A75
Mobasher, B., Dahlen, T., Ferguson, H. C., et al. 2015, ApJ, 808, 101
Morishita, T., Trenti, M., Stiavelli, M., et al. 2018, ApJ, 867, 150
Moster, B. P., Naab, T., & White, S. D. M. 2018, MNRAS, 477, 1822
Moster, B. P., Somerville, R. S., Maulbetsch, C., et al. 2010, ApJ, 710, 903
Moster, B. P., Somerville, R. S., Newman, J. A., & Rix, H.-W. 2011, ApJ, 731, 113
Moustakas, J., Coil, A. L., Aird, J., et al. 2013, ApJ, 767, 50
Murray, S. G., Power, C., & Robotham, A. S. G. 2013, A&C, 3, 23
Muzzin, A., Marchesini, D., Stefanon, M., et al. 2013, ApJ, 777, 18
Oesch, P. A., Bouwens, R. J., Illingworth, G. D., et al. 2012, ApJ, 759, 135
Oesch, P. A., Bouwens, R. J., Illingworth, G. D., et al. 2014, ApJ, 786, 108
Oesch, P. A., Bouwens, R. J., Illingworth, G. D., et al. 2015, ApJ, 808, 104
Oesch, P. A., Bouwens, R. J., Illingworth, G. D., Labbé, I., & Stefanon, M. 2018, ApJ, 855, 105
Oesch, P. A., Brammer, G., van Dokkum, P. G., et al. 2016, ApJ, 819, 129
Oesch, P. A., Labbé, I., Bouwens, R. J., et al. 2013, ApJ, 772, 136
Oke, J. B., & Gunn, J. E. 1983, ApJ, 266, 713
Ono, Y., Ouchi, M., Mobasher, B., et al. 2012, ApJ, 744, 83
Park, J., Mesinger, A., Greig, B., & Gillet, N. 2019, MNRAS, 484, 933
Pei, Y. C. 1993, ApJ, 404, 436
Pérez-González, P. G., Rieke, G. H., Villar, V., et al. 2008, ApJ, 675, 234
Planck Collaboration, Ade, P. A. R., Aghanim, N., et al. 2014, A&A, 571, A16
Planck Collaboration, Ade, P. A. R., Aghanim, N., et al. 2016, A&A, 594, A13
Pozzetti, L., Bolzonella, M., Zucca, E., et al. 2010, A&A, 523, A13
Reddick, R. M., Wechsler, R. H., Tinker, J. L., & Behroozi, P. S. 2013, ApJ, 771, 30
Reddy, N., Dickinson, M., Elbaz, D., et al. 2012, ApJ, 744, 154
Rees, M. J., & Ostriker, J. P. 1977, MNRAS, 179, 541
Roberts-Borsani, G. W., Bouwens, R. J., Oesch, P. A., et al. 2016, ApJ, 823, 143
Roberts-Borsani, G. W., Ellis, R. S., & Laporte, N. 2020, MNRAS, 497, 3440
Rodríguez-Puebla, A., Behroozi, P., Primack, J., et al. 2016, MNRAS, 462, 893
Rogers, A. B., McLure, R. J., Dunlop, J. S., et al. 2014, MNRAS, 440, 3714
Romano, M., Cassata, P., Morselli, L., et al. 2020, MNRAS, 496, 875
Romeo, A. B., Agertz, O., & Renaud, F. 2020, MNRAS, 499, 5656
Salmon, B., Coe, D., Bradley, L., et al. 2018, ApJL, 864, L22
Salpeter, E. E. 1955, ApJ, 121, 161
Schaerer, D., & de Barros, S. 2009, A&A, 502, 423
Schaerer, D., & de Barros, S. 2010, A&A, 515, A73
Schechter, P. 1976, ApJ, 203, 297
Schmidt, M. 1968, ApJ, 151, 393
Scoville, N., Aussel, H., Brusa, M., et al. 2007, ApJS, 172, 1
Shipley, H. V., Lange-Vagle, D., Marchesini, D., et al. 2018, ApJS, 235, 14
Smit, R., Bouwens, R. J., Labbé, I., et al. 2014, ApJ, 784, 58
Song, M., Finkelstein, S. L., Ashby, M. L. N., et al. 2016, ApJ, 825, 5
Stark, D. P. 2016, ARA&A, 54, 761
Stark, D. P., Ellis, R. S., Bunker, A., et al. 2009, ApJ, 697, 1493
Stark, D. P., Ellis, R. S., Charlot, S., et al. 2017, MNRAS, 464, 469
Stark, D. P., Schenker, M. A., Ellis, R., et al. 2013, ApJ, 763, 129
Stefanon, M., Bouwens, R. J., Labbé, I., et al. 2017, ApJ, 843, 36
Stefanon, M., Bouwens, R. J., Labbé, I., et al. 2021a, arXiv:2103.06279
Stefanon, M., Labbé, I., Bouwens, R. J., et al. 2019, ApJ, 883, 99
Stefanon, M., Marchesini, D., Muzzin, A., et al. 2015, ApJ, 803, 11
Stefanon, M., Labbe, I., Oesch, P., et al. 2021b, ApJ, in press
Strait, V., Bradač, M., Coe, D., et al. 2020, ApJ, 888, 124
Sun, G., & Furlanetto, S. R. 2016, MNRAS, 460, 417
Tacchella, S., Bose, S., Conroy, C., Eisenstein, D. J., & Johnson, B. D. 2018, ApJ, 868, 92
Talia, M., Cimatti, A., Giulietti, M., et al. 2021, ApJ, 909, 23
Tasitsiomi, A., Kravtsov, A. V., Wechsler, R. H., & Primack, J. R. 2004, ApJ, 614, 533
Trujillo-Gomez, S., Klypin, A., Primack, J., & Romanowsky, A. J. 2011, ApJ, 742, 16
Vale, A., & Ostriker, J. P. 2004, MNRAS, 353, 189
Vulcani, B., Trenti, M., Calvi, V., et al. 2017, ApJ, 836, 239
Wang, T., Elbaz, D., Schreiber, C., et al. 2016, ApJ, 816, 84
Wang, T., Schreiber, C., Elbaz, D., et al. 2019, Natur, 572, 211
Wechsler, R. H., & Tinker, J. L. 2018, ARA&A, 56, 435
White, S. D. M., & Rees, M. J. 1978, MNRAS, 183, 341
Wilkins, S. M., Bouwens, R. J., Oesch, P. A., et al. 2016, MNRAS, 455, 659
Wilkins, S. M., Feng, Y., Di Matteo, T., et al. 2017, MNRAS, 469, 2517
Williams, C. C., Labbe, I., Spilker, J., et al. 2019, ApJ, 884, 154
Williams, C. C., Maseda, M., Tacchella, S., et al. 2021a, JWST Proposal
Williams, C. C., Oesch, P., Barrufet, L., et al. 2021b, JWST Proposal
Windhorst, R. A., Cohen, S. H., Hathi, N. P., et al. 2011, ApJS, 193, 27
Wyithe, J. S. B., Yan, H., Windhorst, R. A., & Mao, S. 2011, Natur, 469, 181

Yabe, K., Ohta, K., Iwata, I., et al. 2009, ApJ, 693, 507
Yan, H., Dickinson, M., Eisenhardt, P. R. M., et al. 2004, ApJ, 616, 63
Yan, H., Dickinson, M., Giavalisco, M., et al. 2006, ApJ, 651, 24
Yang, X., Mo, H. J., & van den Bosch, F. C. 2003, MNRAS, 339, 1057
Zackrisson, E., Bergvall, N., & Leitet, E. 2008, ApJL, 676, L9

Zackrisson, E., Rydberg, C.-E., Schaerer, D., Östlin, G., & Tuli, M. 2011, ApJ, 740, 13
Zheng, W., Postman, M., Zitrin, A., et al. 2012, Natur, 489, 406
Zhu, H., Avestruz, C., & Gnedin, N. Y. 2020, ApJ, 899, 137
Zitrin, A., Labbé, I., Belli, S., et al. 2015, ApJL, 810, L12